MASTERARBEIT / MASTER'S THESIS

Titel der Masterarbeit / Title of the Master's Thesis

„Groundwater flow modelling of stream-aquifer interaction in an influent regime using hydrogeophysical constraints“

verfasst von / submitted by

Arthur Grebenicek, BSc

angestrebter akademischer Grad / in partial fulfilment of the requirements for the degree of

Master of Science (MSc)

Wien, 2017 / Vienna 2017

Studienkennzahl lt. Studienblatt / degree programme code as it appears on the student record sheet:	A 066 815
Studienrichtung lt. Studienblatt / degree programme as it appears on the student record sheet:	Masterstudium Erdwissenschaften
Betreut von / Supervisor:	Univ. Prof. Dr. Thilo Hofmann

Declaration of Originality

I hereby declare that this thesis and the work reported herein was composed by and originated entirely from me. Information derived from the published and unpublished work of others has been acknowledged in the text and references are given in the list of references. No part of this work has been previously submitted to another educational institution or published elsewhere yet.

Vienna, _____ _____

Date Signature

Abstract

Electromagnetic induction (EMI) investigations represent a rapid, non-invasive and inexpensive method to collect spatially dense data for derivation of properties controlling the flow in the shallow subsurface. Stream-aquifer exchange rates are often controlled by a clogging layer, formed by accumulation of fine-grained sediment in the void pore space. EMI measurements were employed, in constant-walking-speed operation along reaches of a losing-disconnected stream during low flow conditions near a bank filtration site, to gain the streambed's apparent electrical conductivity (EC_a) as a measure of its bulk electrical conductance. The objective of this research was to infer infiltration rates by correlating EC_a with co-located, punctual streambed vertical hydraulic conductivity (K_v) measurements, to develop a log-linear K_v-EC_a relationship for subsequent use in the derivation of a spatially variable Cauchy-type boundary condition in a numerical groundwater flow model. The correlation between measured EC_a and K_v was found to be very weak, arguably pronounced due to methodical problems when installing open-bottom infiltration pipes for K_v determination in the partially pebbly streambed. The regression-based model underestimated total stream infiltration rate by 2.5 orders of magnitude, when compared to existing streamflow loss data. Several EC_a-clustered K_v-EC_a relationships, with varying corresponding upper and lower K_v limits, according to reference literature values, were tested. Incremental adjustments of the lower limit allowed matching total numerical infiltration rate and total streamflow loss data. Using this approach, reach-scale inconsistencies between the numerical infiltration rates and the streamflow loss dataset are apparent. However, the reach with highest infiltration rate was found to be in line with the main infiltration zone as delineated by streamflow loss. While reach-accurate EMI-supported derivation of stream-aquifer exchange rates does not seem promising, the results suggest that EMI may be used prior to more time- and resource-consuming field methods such as (spectral) induced polarization imaging, which target more accurate K_v estimation, by indicating strongly infiltrating reaches.

Zusammenfassung

Elektromagnetische Induktion (EMI) stellt eine schnelle, nicht-invasive und kostengünstige Methode dar, um eine große Anzahl an räumlich verteilten Daten zu erfassen und dadurch Aussagen über den elektrischen Fluss im Untergrund abzuleiten. Die Austauschraten von Oberflächenwasser und Grundwasser im Flussbett werden oft durch eine Kolmationsschicht bestimmt, die sich durch eine Ansammlung feinkörniger Sedimente in den Porenzwischenräumen bildet. Über einen Zeitraum von mehreren Tagen wurden EMI Messungen in einem Flussbett mit influenten Verhältnissen (losing disconnected stream) durchgeführt. Die dabei gemessene scheinbare elektrische Leitfähigkeit (EC_a) des Flussbettes wurde mit parallel durchgeführten Infiltrometermessungen, zur Bestimmung der vertikalen hydraulischen Leitfähigkeit (K_v), korreliert. Ziel der Arbeit war es, eine log-lineare K_v-EC_a-Verbindung zu finden und deren Ergebnisse als Cauchy-Randbedingung in ein numerisches Grundwassermodell zu implementieren. Die Regressionsanalyse ergab eine äußerst schwache Korrelation von K_v und EC_a, vermutlich zurückzuführen auf methodische Probleme beim Versuchsaufbau der Infiltrometer. Das resultierende Modell, basierend auf der Regressionsanalyse, unterschätzte die Infiltrationsraten des Flusses, die bei früheren Studien bestimmt wurden, um mehr als 2,5 Größenordnungen. Die EC_a-Werte wurden daraufhin in Cluster mit variablen maximalen und minimalen K_v-Grenzen unterteilt. Nachdem ein maximaler K_v-Wert gefunden wurde, konnte durch eine schrittweise Anpassung der Werte die untere K_v-Grenze ermittelt und die errechnete Gesamtinfiltrationsrate an die gemessene Abflussrate angeglichen werden. Die errechneten Infiltrationswerte der einzelnen Flussabschnitte wichen teilweise stark von den ermittelten Abflussmengen ab, zeigten jedoch eine generelle Übereinstimmung bei der Bestimmung der Hauptinfiltrationszonen. Der Einsatz von EMI-Messungen zur Bestimmung von Infiltrationsraten, über großflächige Flussabschnitte hinweg, scheint nicht zielführend zu sein. EMI stellt jedoch eine schnelle und einfache Methode dar, um potentielle Hauptinfiltrationszonen zu identifizieren. Diese können mit zeitintensiveren aber zuverlässigeren Methoden, wie der (spektral) induzierten Polarisation (IP), weiter untersucht werden.

Acknowledgement

I would first like to thank my supervisor Univ.-Prof Dr. Thilo Hofmann, from the department of environmental geosciences, for presenting me with this interesting thesis and for the opportunity to work and to learn in his department. Furthermore I want to thank Assistant Prof. Dr. Adrian Flores-Orozco, from the department of geophysics at the TU Wien, for introducing me to the topic of hydrogeophysics, for his support and for the equipment his department provided.

I would like to give special thanks to Philipp Höhn, MSc. Without his constant input and guidance, this thesis could not have been realized.

I also want to acknowledge everyone who supported me throughout my years of study and during the process of researching and writing this thesis. Thank you.

Contents

1. Introduction

Groundwater is one of the most important sources for drinking water in many countries, accounting for more than 50% of the global drinking water supply (Zekster and Everett, 2003). Approximately 2 billion people worldwide and 75% of the residents in the European Union depend on groundwater resources for their drinking water supply (EC, 2008; Kemper, 2004). The major resources for groundwater are shallow alluvial aquifers in river valleys consisting of layers or layered sequences of unconsolidated sediment material (Bertin and Bourg, 1994; Regli et al., 2003; Hiscock, 2014). Recharge is mainly controlled by replenishment from precipitation and infiltration of river water (Bichler et al. 2016).

Transport of shallow subsurface fluids is mainly governed by biogeochemical and physical processes, usually within a highly heterogeneous subsurface of variable soils and sediments. These processes are complex and merely observable and thus limit our ability to understand, predict and to manage shallow systems in a viable manner (Binley et al., 2015). Prediction of groundwater movement and aquifer properties depend largely on the knowledge of hydraulic conductivity (K). Traditional point-scale sampling of subsurface properties (e.g. permeability) and system states (e.g. redox potential, water content, ion concentration) is widely used, often based on invasive drilling approaches including pumping tests, the installation of stationary fluid sampling apparatus (infiltrometer measurements) and the recovery of samples (e.g. core samples used for grain-size analyses). While these methods may be performed relatively easy in the near sub-surface, they are invasive, have relatively high financial and labor costs when investigations have to be extended to greater depths and only provide local information which has to be integrated over a large spatial scale. Therefore large networks of wells are needed to capture effects of spatial distribution and to ensure a high and precise resolution. The increasing complexity of 2D/3D flow and transport models requires distributions of K estimates that are typically only available at very well characterized sites. In some instances, these invasive sampling methods are restricted due to environmental protection constraints (e.g. drinking water production), the threat of disturbing contaminant transport pathways or the inaccessibility caused by infrastructure (Binley et al., 2015).

Hydrogeophysics provide a suitable tool for supporting investigations of the shallow subsurface, to research and predict the dynamics of hydrogeological processes and to ultimately manage groundwater systems. Geophysical investigations, such as electromagnetic induction (EMI), represent non-invasive, inexpensive methods to collect large amounts of data at a large spatial scale, in a relatively short time. Based on the assumption that electrical currents pass through the rock matrix because of water/moisture present in the pores, electrical measurements are mainly influenced by porosity and fluid resistivity. Since flow is also predominantly controlled by porosity, a good estimation

of hydraulic conductivity of a clogging layer in the context of stream-aquifer interactions from surface geophysical measurements could provide important complementary information (Niwas, Tezkan & Israil, 2011).

At the present investigation site a losing-disconnected stream has developed. In disconnected aquifer systems a layer of lower permeability (i.e. clogging or colmation layer) usually forms underneath the losing-disconnected stream. This clogging layer can be very heterogeneous and unevenly distributed amongst/inside the streambed. This thesis involves a numerical groundwater flow model, designed for increasing the understanding of the processes of groundwater (GW)-surface water (SW) interactions at a bank filtration site. Spatially distributed geophysical data from electromagnetic induction measurements (EMI) will be compared to collected vertical hydraulic conductivity (K_v) values from in-stream open bottom pipe measurements. Existing data on infiltration rates and from near-stream observation wells will be used to constrain geophysically inferred exchange rates. The aim is to examine the usability of geophysically estimated data in a Cauchy-type boundary condition for low flow conditions.

2. State of Research

First studies into losing streams concerned the extraction of stream water by groundwater pumping from a nearby well. Theis (1941) developed an analytical model of stream reduction with a vertical streambed and a river fully penetrating an aquifer. Hantush (1965) refined Theis´ model by introducing a vertical semipervious layer along the border of the stream as an analogy to what is known today as clogging layer. This was further developed by Hunt (1990) with a stream not fully penetrating the aquifer underlain by a semipervious layer. However, Fox and Dunford (2003) showed that none of these analytical solutions were suitable for unsaturated flow conditions and explicitly considered the formation of an unsaturated zone beneath a stream, after lowering the water table due to groundwater extraction. Fox and Dunford (2003) proposed that an unsaturated zone beneath a stream would only develop if the material of the streambed was less permeable than the underlying aquifer and developed a method to determine the connection status of a river. It was highlighted that, when the formation of an unsaturated zone occurs, the stream changes from constant head to constant flux boundary condition, with respect to the stream-aquifer system (Irvine, 2010 after Fox and Dunford, 2003). Fox and Dunford (2003) assumed a lower hydraulic conductivity for the streambed by two orders of magnitude, with respect to the aquifer, and took only homogeneous conditions into account, heterogeneity was not considered. Brunner et al. (2009) developed a more precise criterion required for a stream to become disconnected and found a linear relationship between the hydraulic conductivity of the clogging layer and the distance between the base of the clogging layer and the water table where full disconnection occurs. Like Fox and Dunford (2003) and previous researchers, Brunner et al. (2009) restricted their analysis to homogeneous conditions. In recent years, an increasing number of research was performed including streambed heterogeneity in disconnected streams at the stream reach scale (e.g. Cardenas and Zlotnik (2003), Cardenas et. al (2004) Fleckenstein et al. (2006) and Frei et al. (2009)).

Although recent studies started to implement spatial heterogeneity into their models (e.g. Fleckenstein et al. (2006)), Frei et al. (2009) showed that heterogeneity, independent of the depth to the adjoining water table, allows for the simultaneous existence of saturated and unsaturated flow (Irvine et al., 2012). Streambed materials are commonly characterized by means of homogeneous values, derived from calibration or lumped parameters, including stream-geometry and hydraulic properties (Chen et al. 2008).

Controls on losing disconnected streams

Lowering of the groundwater table can cause reductions in streamflow and drying of wetlands (Sophocleus, 2000). Thus, changes in the groundwater table can affect infiltration from surface water bodies (Brunner et al, 2009). The extent to which lowering the water table affects the groundwater

body depends largely on the state of hydraulic connection. In general, two different flow regimes can be found: the streams gains water from inflow of groundwater through the streambed (gaining stream) or the stream loses water to the aquifer (losing stream) (Brunner et al., 2009). In a connected stream-aquifer system there exists no unsaturated zone beneath the stream and streamwater infiltrates directly into the aquifer. In a disconnected stream system, an unsaturated zone develops and infiltrating water must pass through this zone to reach the aquifer. Brunner et al. (2009) refer to this zone, immediately above the water table, as capillary zone. In this zone, saturation, hydraulic conductivity and pressure decrease with increasing distance to the water table of the aquifer. This is not to be mistaken with the term capillary fringe, which describes the region immediately above the water table in which the pressure is greater than the air entry volume (Brunner et al., 2009). Figure 1a and Figure 1b schematically display the flow regimes for a connected and disconnected stream, respectively:

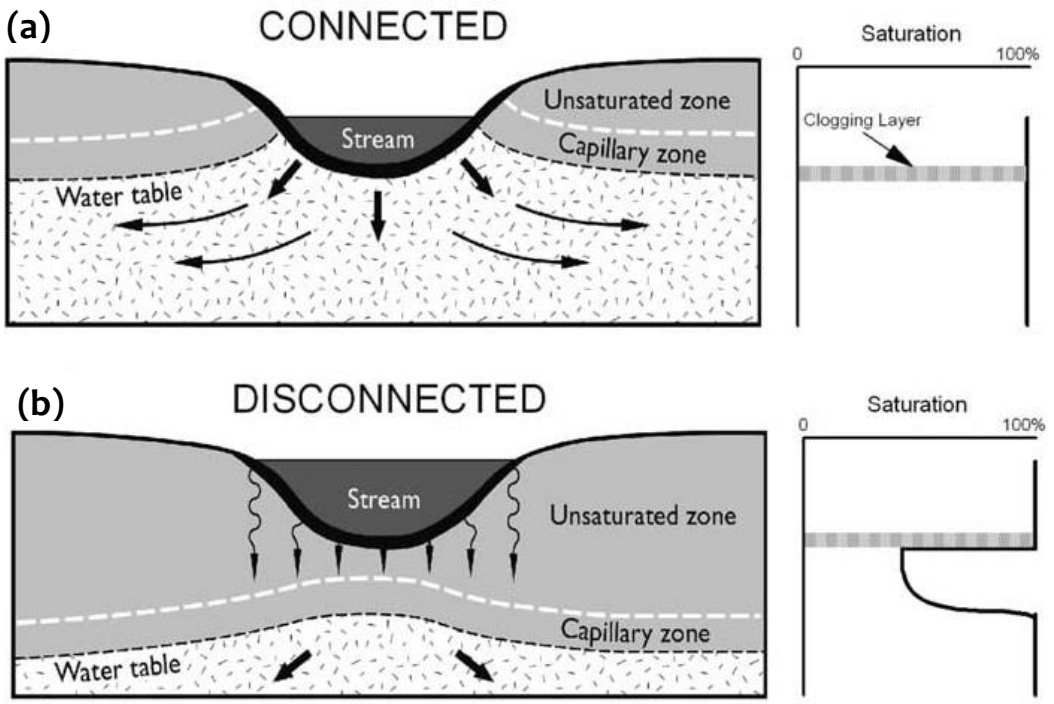

Figure 1. *Different flow regimes of a stream system and its corresponding profile of saturation. (a) Fully connected stream, completely saturated. (b) disconnected stream with constant saturation between the bottom of the clogging layer and the top of the capillary zone (from Brunner et al. 2009, based on Winter et al. 1998).*

Multiple assumptions have been made by researchers to assess whether a stream is disconnected or connected: e.g., the occurrence of a less permeable streambed compared to the underlying aquifer (Fox and Dunford, 2003), the suggestion that disconnection can be linked to the ratio of the stream width to the depth to groundwater (Sophocleus, 2002) or soil properties as well as the head gradient

in the channel (Bouwer and Maddock, 1997). Brunner et. al. (2009) proposed that whether a system can potentially be disconnected, is based on the existence of a clogging layer and depends on the ratio of the hydraulic conductivity of the clogging layer and the aquifer compared to the ratio of the clogging layer thickness and depth of water (height of the water column) above the streambed.

Clogging layer

A clogging layer forms through chemical (mineral precipitation, gas entrapment), biological (biofilm formation) or physical processes (colmation) where, in the latter, fine sediment particles (<2mm), transported with the streamflow, accumulate in the pore space of the uppermost part of the streambed and cause blockages of the porous system (Veličković, 2005). This results in a reduction of pore volume and a significant decrease of permeability (Schaelchli, 1993). Reduced pore volume decreases hydraulic conductivity and results in reduced infiltration rates (Bouwer, 2002; Treese et al., 2009). The clogging layer therefore controls the exchange rate between the stream and the adjacent aquifer (Doppler, 2007). The formation of a clogging layer through accumulation of sediments in the void pore space is indicated schematically in Figure 2.

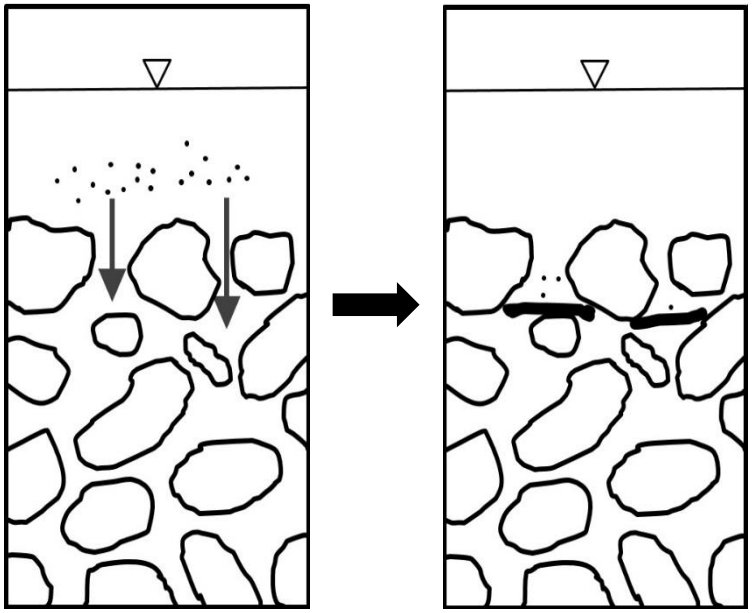

Figure 2. *Conceptual formation process of a clogging layer comprising fine sediment material at the bottom of a streambed. The streambed can be fully or just partially colmated due to heterogeneities.*

When fully connected, the relation between head difference and infiltration flux is linear and the pressure beneath the clogging layer must be greater than zero. Lowering the groundwater table results in the development of an unsaturated zone beneath the clogging layer and negative pressure at the base of the clogging layer. Further lowering the water table increases the negative pressure and the

infiltration flux rate increases asymptotically until approaching a constant value (Figure 3, right) (Brunner et al., 2009). Additional lowering of the water table will not significantly increase the infiltration rate (Bouwer and Maddock, 1997). The system is said to be disconnected (Figure 3, left).

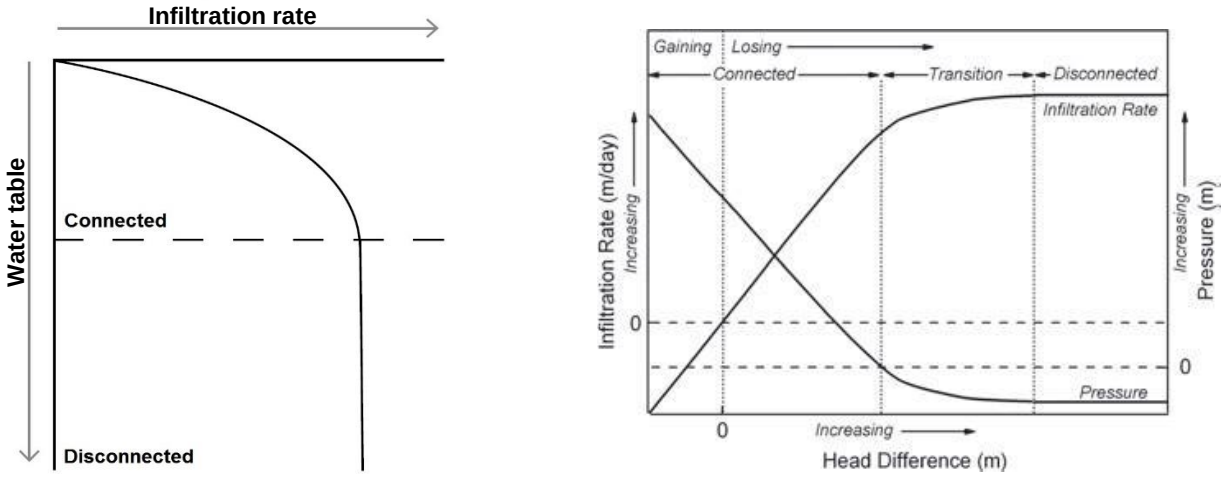

Figure 3. *<u>left</u>: the infiltration rate is proportional to the hydraulic head gradient. When fully disconnected, the infiltration rate is no longer linear but remains relatively constant; <u>right</u>: under gaining conditions (negative head difference) the head pressure is positive. If the head difference is zero, no exchange takes place. If the stream water table is lowered below the stream stage, the pressure drops below zero and an unsaturated zone begins to develop under the clogging layer. (left: from Brunner et al. 2009; right: from Brunner et al. 2010)*

Exchange flows between stream water and aquifer depend on the hydraulic head in the aquifer, the hydraulic head in the river and the hydraulic properties of the clogging layer present in the streambed. As the hydraulic conductivity of the clogging layer is numerous orders of magnitude lower than the hydraulic conductivity of the aquifer, the clogging layer therefore limits the leakage rate (i.e. exchange rate). A modified Darcy equation (Eq. 1) will be used to implement stream-aquifer exchange rates into an existing numerical groundwater flow model as a Cauchy-type boundary condition, according to the leakage principle (e.g. Doppler et al. 2007):

$$q = \frac{K_z \cdot (h_0 - h)}{d_{clogging\ layer}} \qquad \text{(Eq. 1)}$$

where q is the exchange flow per horizontal unit area of streambed, K_z and $d_{clogging\ layer}$ are the vertical hydraulic conductivity and the thickness of the clogging layer, h_0 is the hydraulic head of the

river and h the hydraulic head of the groundwater. The leakage coefficient, as part of Eq. 1, can be expressed as $L = \frac{K_z}{d_{clogging\ layer}}$ (Doppler et al., 2007).

It is widely recognized that exchange fluxes between streams and aquifers can show a high degree of spatial and temporal diversity, often associated to the spatial heterogeneity of hydraulic parameters of the streambed and the adjoining aquifer (Kurtz et al. 2013). Springer et al. (1999) found hydraulic conductivity, measured at reattachment bars in Colorado River, to vary by over two orders of magnitude over a range of 200 miles. Genereux et al. (2008) determined K with permeameter tests along a 262m long river reach and observed streambed hydraulic conductivity to vary by nearly four orders of magnitude. Thus, simplified models cannot completely and realistically display the full hydrodynamic complexity in groundwater - surface water interactions in natural environments and are not applicable to represent highly heterogeneous streambeds when investigated at local scales (Cardenas et al., 2004). Kurtz et al. (2013) consider the determination of the necessary complex for groundwater flow models an open research question and recommend a geostatistical inversion approach, where streambed property changes are applied at the grid cell scale.

Various methods have been developed to gather on-site streambed hydraulic conductivity information and to quantify stream-aquifer interactions. Among the most common are discrete point measurements, using numerous forms of hydraulic tests (e.g. Springer et al., 1999; Chen, 2000), conservative or reactive tracer tests (Leibundgut, Maloszewski & Külls, 2009; Turnadge & Smerdon, 2014) differential discharge gauging and distributed temperature sensing (González-Pinzón et al., 2015).

Geophysical field methods pose a considerable alternative over these common methods to quantify stream-aquifer interactions. Numerous geophysical techniques are currently used in various hydrological investigations. Electrical methods using electrodes with capacitive or galvanic contact with the shallow subsurface (≤10m) including direct current resistivity (DC), induced polarization (IP), spectral induced polarization (SIP) and self potential (SP). First electrical methods were originally developed for ore and resource exploration but soon were deployed for alternative investigation targets and in other configurations, e.g. in boreholes (Daily et al., 1992; Singha and Gorelick, 2005), lysimeter studies (Binley et al., 1996; Koestel et al., 2008) and waterborne studies (Slater et al., 2010).

Another method, ground-penetrating radar (GPR), uses high-frequency electromagnetic waves whose propagation is determined by soil EM-properties and their spatial distribution (Lambot et al., 2006). It detects signals directly transmitted between antennas at shallow depths or reflected signals from the deep underground (Binley et al. 2015). In areas of unsaturated soil conditions GPR is used to e.g. estimate soil water content, locate water tables and map soil stratigraphy. Although a promising tool

to rapidly investigate the shallow subsurface at field-relevant scales, GPR has to undergo extensive and time consuming forward and inverse modelling procedures before being implemented into a workflow involving other qualitative and quantitative information.

Electromagnetic (EM) methods, like electromagnetic induction (EMI), measuring "apparent" or "bulk" electrical conductivity (EC_a), had a great impact over the last decades and are considered the most valuable measurement method characterizing soil spatial variability at field and landscape scale by Corwin (2008) and Lück et al. (2009). EMI can be deployed on the ground surface (manually carried or using a tow platform), in boreholes or airborne, as well as mounted onto a helicopter or a plane. Their wide range of applications and greater and faster scale of investigation, compared to electrical methods, offer distinct advantages over traditional invasive methods as well as time and stationary dependent methods (Doolittle et al., 2014; Binley et al., 2015)

Table 1. *Described geophysical methods, the geophysical properties these methods provide and hydro(geo)logical states derived from the geophysical properties (after Binley et al. 2015).*

Geophysical Method	Geophysical Properties	Derived States/Properties
Direct current Resistivity (DC)	Electrical conductivity	Water content, clay content, pore water conductivity
Induced polarization (IP)	complex electrical conductivity, chargeability	Water content, clay content, pore water conductivity, surface area permeability
Spectral Induced Polarization (SIP)	complex electrical conductivity, chargeability (frequency dependant)	Water content, clay content, pore water conductivity, surface area permeability
Ground penetrating radar (GPR)	Permittivity, electrical conductivity	Water content, porosity, soil stratigraphy
Self-potential (SP)	Electrical sources, electrical conductivity	Water flux, permeability
Electromagnetic induction (EMI)	Electrical conductivity	Water content, clay content, salinity, recharge rate

EMI sensors

First research on effective (bulk) electrical properties of soils was performed at the end of the 19th century (e.g. Briggs, 1899; Wenner, 1915; Archie, 1942) leading to the investigation of effective (apparent) electrical conductivity (EC_a) in the late 1970s for the assessment of soil salinity in agricultural studies (e.g. Corwin and Rhoades, 1982; de Jong et al. 1979; Rhoades and Corwin, 1981; Williams and Baker, 1982). In 1976, Geonics Limited developed and patented the EM31 meter with a depth of investigation (DOI) of 3m and 6m. In 1980, the EM38 was manufactured with a DOI of 0.75m and 1.5m to capture shallow subsurface conditions (Doolittle et al. 2014). EMI investigations were commonly conducted in a station to station mode with an operator walking within a gridded area. In the later half of the 1980s, data loggers were coupled with EM-meters and a rapid collection of geo-referenced EMI data was made available using mobile slays towed by trucks or cars (Cannon et al., 1994; Carter et al., 1993). A growing demand for simultaneous measurements led to the development of dual-dipole sensors to simultaneously measure EC_a and magnetic susceptibility. In 1998, the DUALEM-4 sensor (Dualem, Inc., Milton, Ontario) was developed to provide a DOI of 2m and 6m in both horizontal and vertical dipole orientation. Several advantages were made in recent years, leading to the development of multi-frequency EM-meters with multiple transmitter and receiver coils (e.g. CMD-MiniExplorer, Gf-instruments, CZ;) to collect data simultaneously at different depths using different frequencies.

EC_a and soil properties

According to McNeill (1980), the principal properties influencing EC_a are the type and concentration of ions in solution, the clay content, the water content and the temperature and phase of the soil water (Doolittle et al. 2014). Friedman et al. (2005) further categorized three major groups: (i) structure, water content (θ) and porosity (*n*); time-invariable solid particles: (ii) particle shape and orientation, particle size and cation exchange capacity (CEC); (iii) cation composition, ionic strength and temperature. These ancillary properties, which can be very complex and often vary over short distances, can indirectly influence soil EC_a properties (Doolittle et al. 2014; Brevik et al. 20014). As a result, extensive research has been conducted to link EC_a to the properties mentioned above: Johnston et al. (1997) and Mankin and Karthikeyan (2002) found that the concentration of soluble salts is the dominant factor in salt-affected soils (Doolittle et al., 2014). EMI has been used to map salt content across landscapes (Williams et al., 2006; Cook et al. 1989a), evaluate rates of groundwater recharge (Cook et al., 1989a, 1989b, 1992), indicate unsaturated flow (Scanlon et al., 1999) and map groundwater discharge and recharge zones (Richardson and Williams, 1994) (Doolittle et al., 2014). Apparent conductivity has also been used to link to soil texture (e.g. James et al., 2003; Saey et al. 2012; White et al., 2012), water content (e.g. Kean et al., 1987; Sheets and Hendrickx, 1995; Brevik and

Fenton, 2002; Brevik et al., 2006; Allred et al., 2005), soil pH (e.g. Dunn and Beecher, 2007; Vithrana et al., 2008; Wienhold and Doran, 2008), CEC (Korsaeth et al., 2008; Triantafilis et al., 2009) and for lithological (e.g. Boucher et al., 2012) and hydraulic characterization at aquifer scales(e.g. Camporese et al., 2011).

Little, however, is known about the feasibility of hydrogeophysics to estimate recharge or discharge rates. Cook et al. (1992) used frequency-domain (FDEM) and time-domain (TDEM) EM instruments to estimate spatial patterns of groundwater recharge at a semi-arid field site in south eastern Australia. They found that there was an inverse relationship between recharge rate and subsurface electrical conductivity for FEM instruments and that this was due to the correlation of recharge and soil texture. They further argued, as recharge is mainly affected by shallow subsurface soil texture, that hydrogeophysical methods and instruments sensitive to the shallow subsurface would be the most favourable in investigating recharge. Cook and Kilty (1992) illustrated the applicability of large-scale helicopter-borne surveys for mapping recharge rates and pointed out that there is little to no loss of accuracy, compared to surface surveys, and that electromagnetic methods can provide detailed information on recharge processes. Khan et al. (2009) performed electromagnetic surveys along horizontal drainage wells and established a connection between EC_a and infiltration rate measured using seepage meters. Crosbie et al. (2014) conducted a survey using a floating resistivity array (vertical electrical sounding – VES) at a disconnected ephemeral creek and derived estimates of river loss using a simplified infiltration model. Both, Khan et al. (2009) and Crosbie et al. (2014) showed high uncertainty regarding the inferred loss rate.

Thus, geophysical methods are considered likely to have the highest potential to aid in extrapolating small-scale measurements, especially in disconnected streams, but considerable research efforts on this topic have yet to be performed to produce further reliable results (Cook 2015).

3. Material & Methods

3.1 Groundwater flow

The understanding of hydraulic relationships between streams and adjoining aquifers, which is crucial in water resource management, depends strongly on the knowledge of streambed hydraulic conductivity (K) (Chen, 2000). The hydraulic conductivity describes the ease of movement of water through a porous material and depends upon the porosity (n) of a porous aquifer, more precisely on the effective porosity (n_e) or specific yield, which can be determined as the portion of total void space capable of transmitting fluid (Practical and Applied Hydrogeology, 2015).

Laminar groundwater flow within an aquifer can be described by Darcy´s law:

$$Q = K \cdot A \frac{(h_1 - h_2)}{L} \quad \text{(Eq. 2)}$$

where the total flow rate, Q [$m^3\ s^{-1}$], is proportional to the difference in water level h_1-h_2 [m] and the cross-sectional area, *A* [m^2], and inversely proportional to the horizontal distance L [m]. K [$m\ s^{-1}$] is the hydraulic conductivity of the porous material.

Eq. 2 can be rewritten into:

$$\frac{Q}{A} = q = K \cdot i \quad \text{(Eq. 3)}$$

where q [$m\ s^{-1}$] is the specific discharge rate and i is the dimensionless hydraulic gradient.

To effectively describe groundwater flow through a porous medium a conservation of mass is considered balancing inflow, outflow and change in water mass (Domenico and Schwartz, 1998). This statement is applied to a theoretical rectangular volume of porous material with sides of length Δx, Δy, Δz and porosity, n. Net outflow can be calculated via the difference between the inflow and outflow through all the faces of the cell and is given by Eq. 4:

$$-\left[\frac{\partial(\rho_w q_x)}{\partial_x} + \frac{\partial(\rho_w q_y)}{\partial_y} + \frac{\partial(\rho_w q_z)}{\partial_z}\right] \Delta x \Delta y \Delta z = \frac{\partial(\rho_w n)}{\partial t} \Delta x \Delta y \Delta z \quad \text{(Eq. 4)}$$

where ρ_w is the density of water, n the unit volume and q_x, q_y, q_z are the flow rates in the respective directions. Dividing both sides by $\Delta x, \Delta y, \Delta z$ and ρ_w, assuming that the density of the fluid does not vary spatially, gives Eq.6. Net outflow rate changes per volume now equals the rate of temporal change of fluid volume and can be applied to anisotropic media (Domenico and Schwartz, 1998). The left-hand side of the equation can be substituted by Darcys´equation constituting Eq.5:

$$-\left[\frac{\partial q_x}{\partial_x} + \frac{\partial q_y}{\partial_y} + \frac{\partial q_z}{\partial_z}\right] = \frac{\partial}{\partial x}\left(K_x \frac{\partial h}{\partial x}\right) + \frac{\partial}{\partial y}\left(K_y \frac{\partial h}{\partial y}\right) + \frac{\partial}{\partial z}\left(K_z \frac{\partial h}{\partial z}\right) \quad \text{(Eq. 5)}$$

where K_x, K_y and K_z is the hydraulic conductivity at respective directions.

Assuming that gains and losses within the considered aquifer volume are proportional to differences

in hydraulic head a proportionally constant is needed to convert head differences to the amount of fluid lost or gained in the cell unit volume. Eq.6 describes this relation, where S_s is the specific storage which is equal to zero at steady state and unequal zero at transient conditions. The left-hand side of Eq.5 can be replaced by Eq. 6.1 and is resulting in Eq. 6.2. The unit of S_s is L^{-1}.

$$S_s \frac{\partial h}{\partial t} = \frac{\partial (n)}{\partial t} \; (1) \; S_s \frac{\partial h}{\partial t} = \frac{\partial}{\partial x}\left(K_x \frac{\partial h}{\partial x}\right) + \frac{\partial}{\partial y}\left(K_y \frac{\partial h}{\partial y}\right) + \frac{\partial}{\partial z}\left(K_z \frac{\partial h}{\partial z}\right) (2) \qquad \text{(Eq. 6)}$$

Assuming homogeneity and isotropic conditions, within the considered volume, Eq. 7 describes a transient hydraulic head field:

$$\frac{S_s}{K}\frac{\partial h}{\partial t} = \frac{\partial^2 h}{\partial x^2} + \frac{\partial^2 h}{\partial y^2} + \frac{\partial^2 h}{\partial z^2} \qquad \text{(Eq. 7)}$$

The equation can be written more concisely by using the Laplace operator resulting into Eq. 8 and Eq. 9:

$$\frac{\partial^2 h}{\partial x^2} + \frac{\partial^2 h}{\partial y^2} + \frac{\partial^2 h}{\partial z^2} = \nabla^2(h) \qquad \text{(Eq. 8)}$$

$$\frac{S_s}{K}\frac{\partial h}{\partial t} = \nabla^2(h) \qquad \text{(Eq. 9)}$$

For transient (i.e. most natural) conditions, the height of the groundwater table is continuously changing and therefore $\nabla^2(h) \neq 0$. At steady state conditions, the height of the groundwater table does not change resulting in $\nabla^2(h) = 0$.

(From “Physical and Chemical Hydrogeology”, Domenico and Schwartz, 1998)

3.2 Measurement of vertical hydraulic streambed conductivity

As widely accepted, porous aquifers and streambeds show large effects of anisotropy and heterogeneity of their spatial hydraulic conductivity and porosity distributions (Hiscock, 2005). Due to depositional and layering processes of sediment material, horizontal conductivity (K_h) is usually larger

than vertical conductivity (K_v) by two orders of magnitude (Chen, 2000). To easily measure vertical hydraulic conductivity of a streambed, Chen (2000) developed an open-bottom standpipe method, similar to that of permeameter methods, performing transient infiltration tests, as described in several textbooks (e.g. Domenico and Schwartz, 1998).

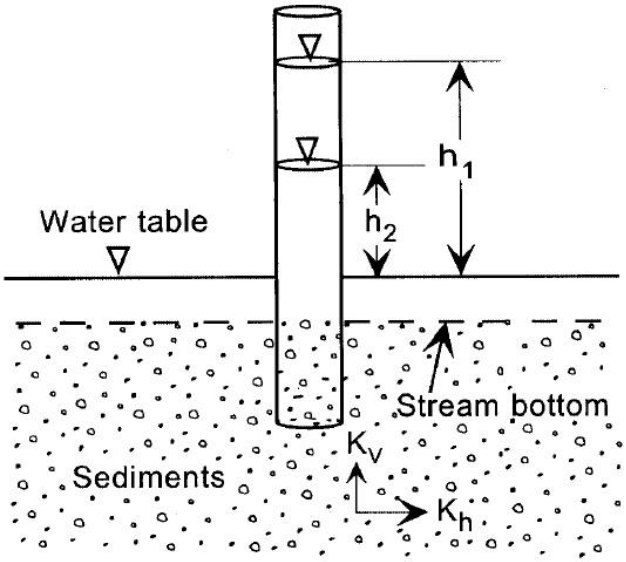

Figure 4. *Schematic diagram of a standing open-bottom infiltrometer, vertically hammered into the stream channel. The lower part is filled with unconsolidated sediment material, the hydraulic head at the bottom of the pipe equals the water level of the stream. Water is poured into the pipe and K_v is calculated using Eq. 10. From Chen, 2000.*

Figure 4 shows an open-bottom pipe pressed vertically into the streambed sediment. Water is poured into the pipe and flows through the sediment column to the bottom of the pipe. The hydraulic head is measured at t_1 and t_2, K_v can then be calculated using Eq. 10:

$$K_v = L_v/(t_2 - t_1)\ln(\frac{h_1}{h_2}) \quad \text{(Eq. 10)}$$

where L_v is the thickness of the streambed in the pipe, h_1 is the hydraulic head in the pipe at time $t_1$and h_2 is the hydraulic head in the pipe at later time t_2.

Hvorslev (1951) developed a formula to calculate K_v in saturated soils:

$$K_v = (\pi D/11m + L_v)/(t_2 - t_1)\ln(\frac{h_1}{h_2}) \quad \text{(Eq. 11)}$$

where D is the diameter of the pipe and $m = (K_h/K_v)^{0.5}$. As two unknown variables are present in Eq. 11 (K_h and K_v) K_v cannot be calculated directly. However, when the length of sediment column (L_v) is several times larger than the diameter of the pipe, Eq. 11 can be approximated using Eq. 10 (Chen, 2000). As horizontal flow also occurs within the sediment inside the standpipe, Eq. 10 will underestimate K_v to a certain degree. Strongly anisotropic streambeds tend to show lower calculation errors. For the current test site an error of ~4%, was calculated, resulting in an uncertainty of K_v in the range of only a single decimal place.

3.3 Geophysical principles and parameters

Electromagnetic induction

Electromagnetic induction meters, like the CMD-2, consist of a transmitter (Tx) and a receiver coil (Rx). The transmitter is energized with a time-varying electric current at audio frequency, inducing a primary electromagnetic field (H_p). The primary electromagnetic (EM) field induces small currents, i.e. eddy currents, in the conductive subsurface, which generate a secondary EM-field (H_s) with opposite polarity and magnitude of the incident primary field. The secondary and primary EM-field are sensed and recorded by the receiver coil at a set distance (r) from the transmitter coil (Figure 5).

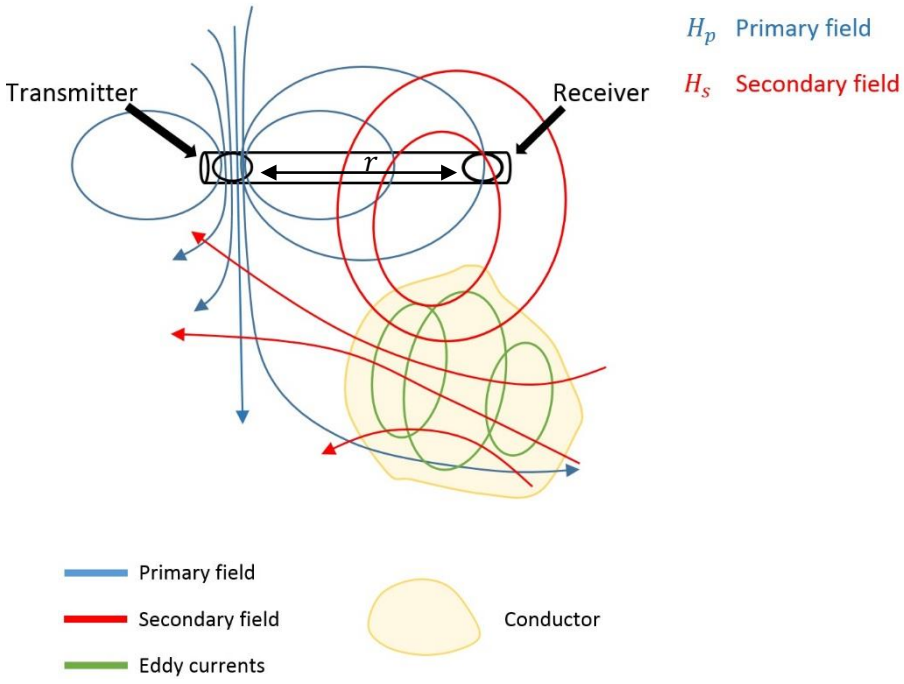

Figure 5. *Schematic representation of an EMI instrument and generated electromagnetic fields*

The generation of the secondary field H_s is a complex function depending on intercoil spacing, r, the operating frequency, f, and the electrical conductivity of the subsurface, σ. When operating at low induction number (LIN), the secondary EM field can be delineated to Eq.12:

$$\left(\frac{H_s}{H_p}\right) \cong \frac{i\omega\mu_0\sigma_a r^2}{4} \qquad \text{(Eq. 12)}$$

where $\sigma_a$is the apparent electrical conductivity, $i = \sqrt{-1}$, $\omega = 2\pi f$ and μ_0 =magnetic permeability. When H_s/H_p is known, the apparent electrical conductivity can be defined as:

$$\sigma_a = \frac{4}{\omega\mu_0 r^2}\left(\frac{H_s}{H_p}\right) \qquad \text{(Eq. 13)}$$

The measured σ_a represents the weighted average of the sediments σ across a depth range, depending on intercoil spacing, r, and their orientation (McNeill, 1980).

The effective depth of exploration (i.e. skin depth) which is based on vertical spatial sensitivity, assuming a homogeneous and horizontally layered half-space model, is given by Eq. 14 (Spies, 1989):

$$b = \frac{r}{\delta} = \frac{r}{\sqrt{\frac{2}{\sigma_a\omega\mu_0}}} \qquad \text{(Eq. 14)}$$

where the induction number, b, is the ratio of the intercoil spacing, r, to the effective depth of exploration, δ. The skin depth is defined as distance in the half-space (i.e. depth) at which the propagating magnetic field amplitude has been attenuated to e^{-1} of its initial amplitude at the surface (Brosten et al., 2011; McNeill 1980). The ratio of H_s/H_p is recorded as in-phase, or *real part*, the quadrature data in parts-per-million (ppm) as out-of-phase, or *imaginary part* (Brosten et al., 2011). The low induction number approximation is especially valid for environments where $b \ll 1$ (e.g. $\sigma_a < 100$ mS m^{-1}), where the information of electrical conductivity is stored within the imaginary component (i.e. quadrature).

Assuming a multi-layered earth response, McNeill (1980) developed a spatial sensitivity analysis using the cumulative electrical conductivity response-function (expressed as % of the measured signal) of the relative contribution to the secondary magnetic field of the soil volume above a certain depth of exploration. Conventionally, depth of exploration is defined where 70-75% of cumulative response is achieved.

As a function of normalized depth, z (actual depth divided by intercoil spacing, r), McNeill (1980) established equations for horizontal coplanar (CS_{HCP}) and vertical coplanar (CS_{VCP}) coil orientations:

$$CS_{HCP}(z) = \int_{z}^{\infty} LS_{HCP}\,(z)dz = \frac{1}{(4z^2+1)^{0.5}} \qquad \text{(Eq. 15)}$$

$$CS_{VCP}(z) = \int_{z}^{\infty} LS_{CVP}(z)dz = (4z^2+1)^{0.5} - 2z \qquad \text{(Eq. 16)}$$

where LS = the local sensitivity. Local sensitivities are derived from the sum of contributed secondary magnetic fields generated at different depth levels, within individual subsurface layers.

Figure 6 shows different sensitivities for HCP and VCP mode configurations. When the coils are aligned vertical coplanar the EMI instrument is most sensitive to near-surface layers, the contribution to the secondary magnetic field therefore decreases fast with increasing depth. In horizontal coplanar mode sensitivities reach their maximum peak at greater depths and are less sensitive to shallow layers. As the investigation depth is solely depending on intercoil-spacing, the CMD-2 (r=1.89m) shows the highest sensitivity at 0-0.5m for VCP mode and 0.3-1.8m for HCP mode, respectively.

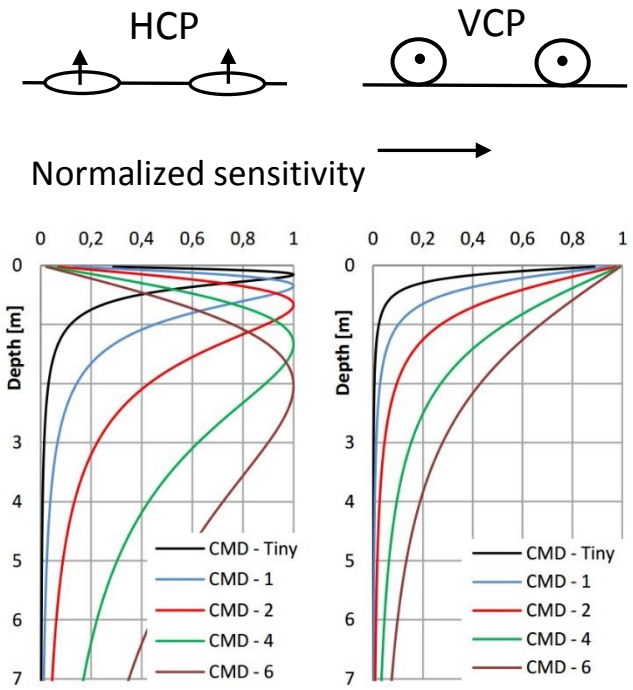

Figure 6. *Normalized sensitivity plotted against depth for different CMD models. left: plot for horizontal coplanar mode; right: plot for vertical coplanar mode. Figure obtained from http://www.gfinstruments.cz/*

Linking apparent electrical conductivity to hydraulic conductivity

Apparent electrical conductivity (σ_a) is a measure of electrical conductance through bulk soil. Three possible pathways contribute to σ_a of a soil: (i) a solid pathway via interconnected grains and minerals (σ_a), (ii) a solid-liquid pathway via the grain surface, mainly in association with clay minerals (σ_s), and (iii) a liquid phase pathway via the fluid in the interconnected pore space (σ_f) (Rhoades et al 1999; Corwin and Lesch, 2005). In the absence of metallic or semiconducting minerals the solid phase of soils and rocks is thought to be non-conducting and can therefore be neglected ($\sigma_a = 0$).

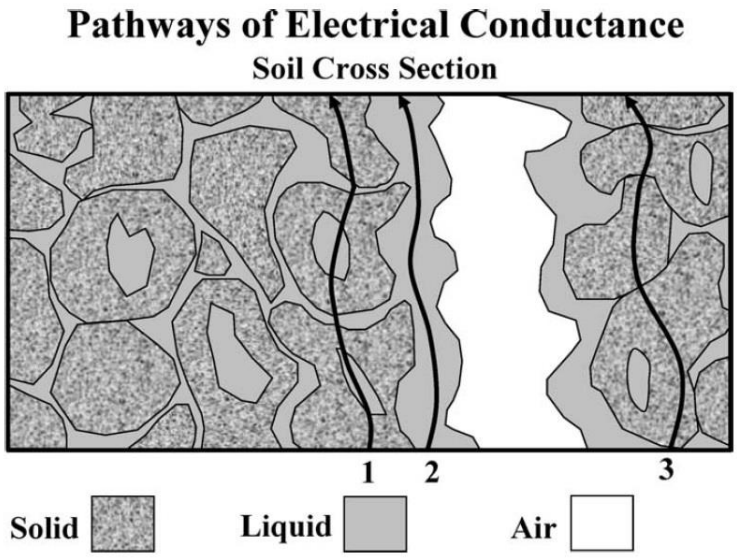

Figure 7. *Schematic concept of the three pathways: (1) solid, (2) liquid, (3) solid-liquid from Corwin and Lesch, (2005) after Rhoades et al. (1989).*

The subsurfaces´ complex electrical conductivity (σ^*) can be expressed by an in-phase electrical conductivity component, or real part (σ') contribution and an out-of-phase electrical conductivity component, or imaginary part (σ'') contribution. The imaginary part can only be detected with induced polarization techniques and was therefore not specifically considered. Electrical conduction (σ') relates to electrolytic conductivity (σ_{el}) of electrolytes (i.e. ions) in the pore-filling fluid and to interfacial conductivity (σ'_{int}) in the electrical double layer at the grain-fluid interface (Slater, 2006). σ' can be expressed as:

$$\sigma' = \sigma_{el} + \sigma'_{int} = \left(\frac{1}{F}\right)\sigma_w + \sigma'_{int} \qquad \text{(Eq. 17)}$$

where σ_w is the electrical conductivity of the pore-filling fluid and F is the so-called formation factor which can be expressed as $F = \sigma^w / \sigma'$ (Archie, 1941).

Although σ'_{int} and σ_{el} can be linked to interconnected pore volume and interconnected surface area, respectively, via petrophysical models, it is not possible to determine the relative weight of the controls of σ'_{int} and σ_{el} on the measured conductivity (σ'). Any relationship between σ' and hydraulic conductivity K, will therefore depend on site specific physical and chemical properties of the soil and the pore-filling fluids (Slater, 2006). Huntley (1986) found a log-log linear relationship between K and $|\sigma| \cong \sigma'$ which can be either positive or negative. Saturated soils with relatively low specific surface area (S_a) (sandy sediments and gravels in absence of clay) are dominated by σ_{el} and show a positive linear log K-log σ' relationship as a result of increasing σ' and K_v, due to increasing porosity (ϕ) (e.g. Heigold et al. 1979; Purvance and Andricevic 2000). A relationship between σ' and effective porosity (ϕ_{eff}) was empirically (Archie 1941) and theoretically (Sen et al., 1981) established, as can be seen in Eq.18:

$$\sigma' \approx \sigma_{el} = \frac{\sigma_w}{F} = \sigma_w \phi_{eff}^m \qquad \text{(Eq. 18)}$$

where m is the cementation exponent ($1.3 < m < 2.4$). The formation factor F can be further expressed as $F = \phi^{-m}$.

However, this positive relationship is only true for sediments with dominating σ_{el}. Sediments with higher S_a (clays and silts) display elevated electrical conductivities due to the formation of an electrical double layer (EDL) surrounding the mineral grain. An excess of negative surface charges results in the accumulation of positive cations in the double layer, hence increasing the electrical conductivity of the clay-rich sediment through ionic migration. It is widely recognized that for highly saturated soils, dominated by σ'_{int} , a negative linear log K-log σ' relationship exists (e.g. Kelly 1977; Ponzini et al. 1983; Purvance and Andricevic 2000). This relationship can be established given the fact that the surface area per unit pore volume (S_{por}) follows an inverse square relation to K (Eq. 18) while σ'_{int} increases with increasing S_a (Slater, 2006). Purvance and Andricevic (2000) explained the positive and negative linear log-log relationship between K and σ', using a modified microscale network model after Bernabe and Revil (1995). They found a positive σ'-K relationship if the current flow was dominated by interconnected pore volume (i.e. σ_{el}) and a negative relationship if the current flow was dominated by interconnected pore surface charge (σ'_{int}) and developed Eq. 19 using theoretically derived relations of K and ϕ as well as σ' and S_a (Slater, 2006):

$$K = a(\sigma')^b \qquad \text{(Eq. 19)}$$

where a is a constant, $\sigma' \approx \sigma_{el}$ and b is the ratio of $\sigma' - \phi$ and K$-\phi$ (b being positive), for pore volume controlled conduction. For pore surface charge controlled conduction $\sigma' \approx \sigma_{int}$ and b is the ratio of $\sigma' - S_a$ (being positive) and K$-S_a$ (being negative). However, a and b have to be estimated from geoelectrical measurements and compared to measured K values. Although σ' can be characterized through the pore volume pathway and the pore surface area pathway, prediction of K is still limited to the fact, that only one of these electrical properties can be inferred (considering the other one insignificant) (Slater, 2006).

3.4 Data acquisition and processing

EMI

Geophysical data was obtained using the CMD-2 electromagnetic conductivity meter as a non-invasive induction-based sensor, manufactured by GF Instruments, s.r.o. The position of the streambed inside the valley prevented accurate GPS location, therefore a Leica TPS1200 tacheometer was used to obtain cartesian coordinates.

The CMD-2 has a set transmitter/receiver distance of 1.89m and can record data either in the horizontal- or vertical-dipole coil configuration. It is capable of measuring two depth ranges either in HIGH or LOW mode with an effective depth range of 3.0m and 1.5m, respectively. The stream was divided into multiple non-uniform segments, depending on the occurrence of several barriers along the river course where no continuous measurement and walking was possible. Each subsegment was divided in three quasi-straight lines x_00, x_02 and x_04 were x_00 was the right side, x_02 the central axis and x_04 the left side of the streambed, facing downstream. At several occasions where water depth exceeded 1m or stream currents were too strong, no measurements were performed.

Coordinates were recorded with the tacheometer at every starting point of each line and whenever a deviation from the straight line occurred due to obstacles or changes in walking direction, depending on river morphology. The measurement mode was set to LOW and “continuous”. Measurement intervals for continuous mode vary between 0.1-1s and were adjusted according to walking velocity, corresponding to approx. 0.7m-1m datapoint spacing along the three lines. The EMI instrument was carried by an operator at a fixed height of 1.1m above the ground surface. To eliminate operator-bias all EMI measurements were performed by the same person.

EMI data was sent to TU Vienna (Technical University) for processing and visualization. A geospatial vector data file (i.e. shapefile created with ArcGIS, Esri, USA) with EMI-datapoints (n=3890) was generated, containing XY-coordinates and apparent electrical conductivity values.

K_v values

Point K_v was determined at random positions along the central axis within three subsections of the river (n=49) with greater EC_a-variability. Pointed open-bottom infiltrometers (100cm long and 4cm in diameter) were hammered vertically into the sediment to a depth of 20-30cm. Diver® water level data loggers were attached inside the metal pipes to measure water pressure. A single Diver® was calibrated as Baro-Diver and placed at an open spot to collect barometric pressure data. As the Diver® inside the pipe measures absolute pressure, the water pressure and the air pressure pushing on the water surface, the Baro-Driver is needed for air pressure compensation. The pipes were filled several times with 5l of stream water to measure hydrostatic head decrease and thus decrease in water pressure. After measuring sediment thickness, in respect to pipe length, K_v was determined using Eq. 11 (see chapter 3.2).

Figure 8. *Left: set up of open-bottom K_v-measurements at the central axis of a stream segment; right: stock picture of the CMD-2 conductivity meter, http://www.gfinstruments.cz, CZ.*

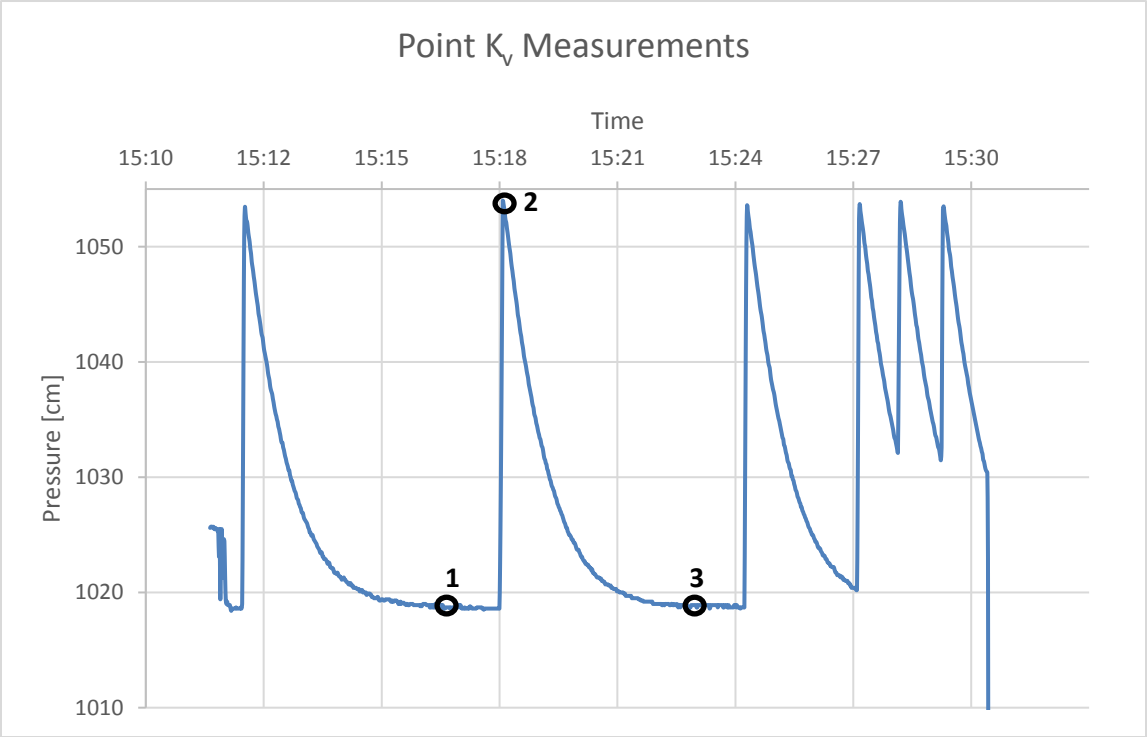

Figure 9. *To calculate K_v from measured Diver data, three data-points have to be picked for every measurement: 1) determination of the baseline, where little to no changes in pressure occur over a course of time; 2) the peak, where pressure reaches the maximum value and 3) where pressure reaches a constant value after the drawdown again (i.e. baseline of the next peak/refill).*

3.5 Numerical Groundwater Model

Site description

The test site is situated in a subalpine headwater catchment, within a valley formed by late glacier activity, during the last ice ages, in western Europe. A synorogenic foreland basin forms the base of the area, overlain by up to 60m of gravel (Bichler et al., 2016). The investigated area is mainly used for agriculture and stock farming. The headwater area is covered by forest (EEA, 2006). Average annual precipitation ranges between 1300mm and 1500mm, with a mean annual air temperature of 8.6°C (Brünjes et al., 2016). The aquifer consists of Pleistocene sediments comprising mainly coarse carbonate gravels with a mean hydraulic permeability of 1.5×10^{-2} m s^{-1}, resulting in a high linear flow velocity of 60-70m d^{-1} (Bichler, Neumann, Hofmann, 2014).

Within the valley two streams exist (A and B) but only stream A infiltrates significantly into the aquifer, where infiltration from stream B was found to be negligible. The total length of stream A within the model area is 4.23km with an average discharge rate of 8.7m^3 s^{-1} (Bichler et al. 2016). A second tributing aquifer exists, recharged insignificantly by stream B. Extraction of groundwater from a nearby horizontal drainage well has resulted in the lowering of the groundwater table below the stream stage

and below the streambed throughout the test site. The depth to groundwater table in this area is between 3-5m below stream stage, having resulted in permanently influent conditions and an unsaturated zone below the streambed (Bichler et al. 2016). Following snowmelt, floods usually occur in spring and throughout the year after heavy rainfall events. Alongside stream A, a dam was built along the entire length of the area to prevent flooding. To prevent erosion, breakwaters have been installed at several points mid-stream. A weir near the southern end of the model domain controls stream discharge. If the stream discharge upstream the weir does not exceed 11.2 $m^3 s^{-1}$, inflow into the model area is approx. 1.2 $m^3 s^{-1}$ (i.e. low flow conditions). An increase in discharge over 11.2 $m^3 s^{-1}$ (i.e. high flow conditions) thus increases streamflow in the investigated stream A, as the capacity of the regulating bypass channel, alongside the weir, is limited at 10 $m^3 s^{-1}$. Tertiary bedrock is found underlying the aquifer, acting as an aquiclude. Parts of this tertiary rock crop out along stream A, preventing infiltration and thus were not considered in the groundwater model.

Model area

The numerical model comprises two aquifers from south to north towards a groundwater extraction well. The modelled area has a maximum extent of 4km in east-west direction and 3.5km in north-south direction. Aquifer A has a length of approximately 3.9km and a width of 0.8 to 1.2km. Aquifer thickness and extent were derived from information and data from various boreholes in this area. The area comprises a partially infiltrating stream. The stream was cut out along a 2km transect due to a layer of marl acting as impermeable boundary.

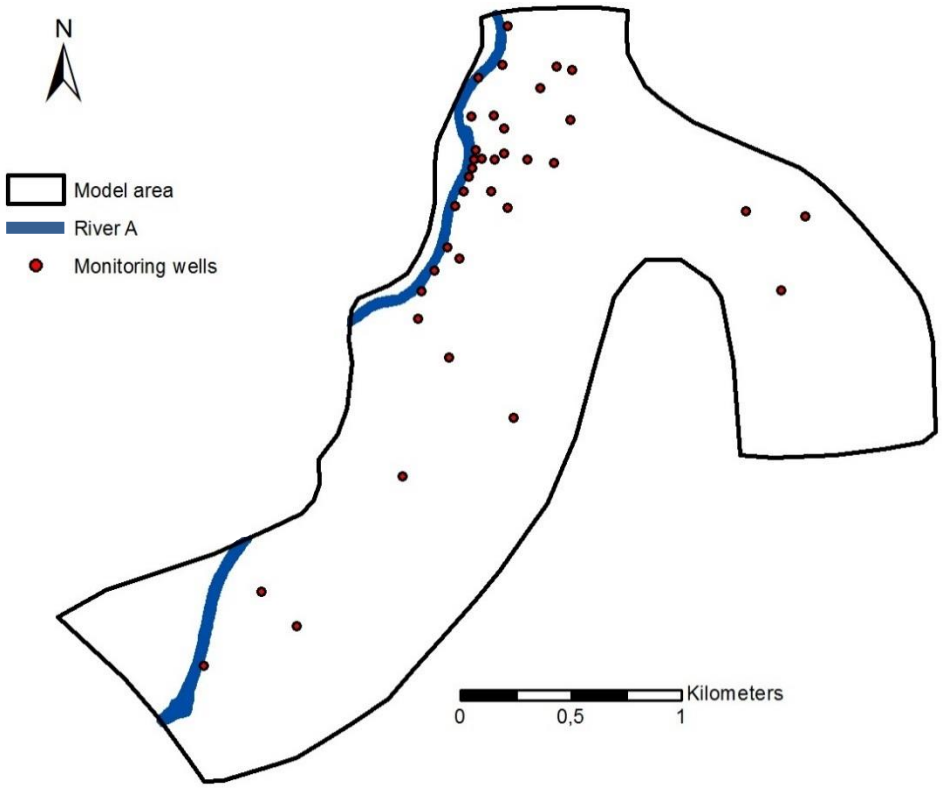

Figure 10. *Model area extent with stream axis and monitoring wells.*

Model setup and pre-processing

A simplified v-shaped 3-dimensional representation of the stream stage was generated using inverse distance weighing (IDW) interpolation with a maximum depth of 1m in the central stream axis and zero depth at the stream embankment boundary. Model area and well sites were provided as geospatial vector data (i.e. shapefile created with ArcGIS, Esri, USA), as a result of earlier research. The streambed was manually digitized from satellite and airborne imaging data.

Subsequently, the digitized streambed was subdivided into a 1x1m raster-grid. The collected EMI data (EC_a) was converted into a point vector dataset and spatially interpolated with IDW within the extent of the streambed to create a continuous raster. At the positions, where the infiltrometer measurements were performed, EC_a values were extracted as point data from the generated raster data. Comparing EC_a and K_v, a logarithmic regression analysis was performed. The best-fitting regression function was used to convert EC_a values to vertical streambed K_v values. The altered values will be implemented into the model to perform flow analysis (and water budget) and to check for probability.

A steady state groundwater flow model based on numerical domain discretization using finite elements was generated to simulate 3-dimensional flow field conditions using FEFLOW (DHI-WASY, Denmark). The numerical model was conceptually based on an existing groundwater flow model of the site. Inverse calibration of hydraulic parameters (i.e. hydraulic conductivity K, and drainable porosity, n_e) was performed by earlier research for quasisteady-state flow conditions with heterogeneity being depicted using kriging between pilot points. The results from this calibration were adopted and included, according to reference literature, the ratio of anisotropy between vertical and horizontal hydraulic conductivity was assumed to be 0.2.

To ensure numerically accurate depiction of hydraulic gradients, the mesh was locally refined near drainage and monitoring wells. To improve mesh quality and to prevent numerical instability, elements had to be refined after initial mesh generation to fulfil the Delaunay criterion: the closer the maximum interior angles are to 60°, the better the mesh quality. Figure 11 shows a comparison of the statistical distribution of maximum interior mesh triangle angles, with and without additional smoothing.

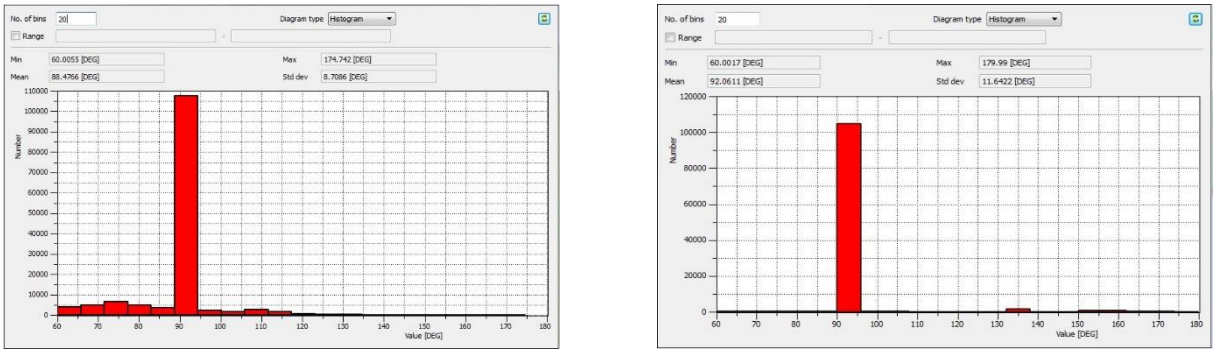

Figure 11. *Parameter statistics for max. interior angle of triangles; left: mesh generated with additional smoothing, right: mesh without smoothing*

Local refinement was particularly prominent at the north-western part of the model where a high density of monitoring wells and the drainage wells are located (see Figure 12, right). The streambed was implemented as raster-grid with a set pixel edge length of 1x1m.

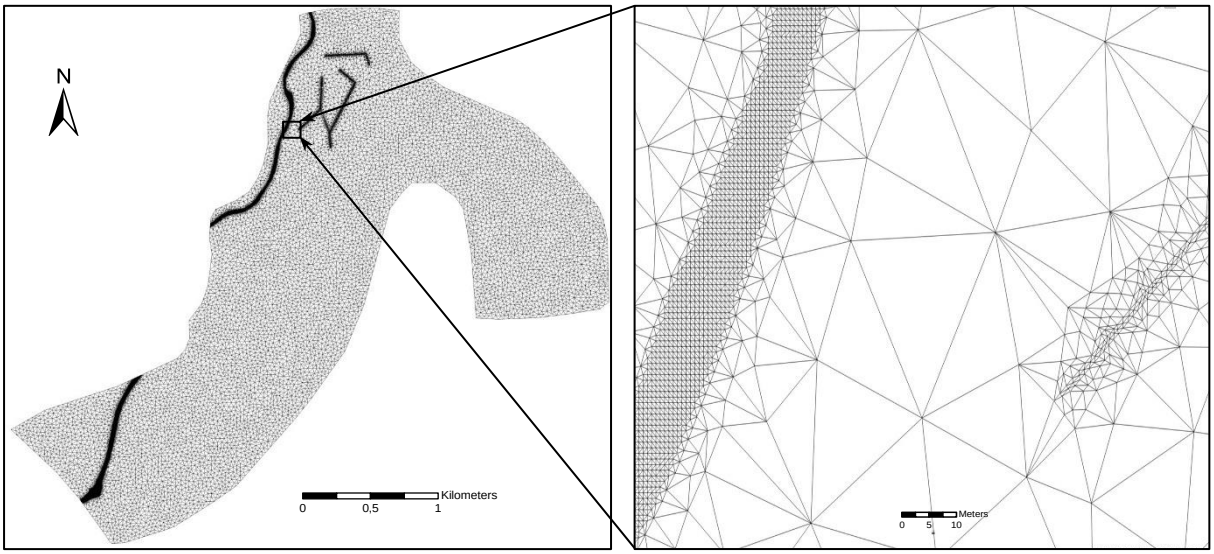

*F*igure 12*. Overview of the model extent with drainage wells and streambed (left); enlarged section of the mesh, showing stream and drainage wells structure (right)*

A total number of 705.815 elements and 425.292 nodes were generated. Every layer containing 141.163 elements and every slice 70.882 nodes.

Layers and Slices

Vertical segmentation was realized using layers and slices. Slices are surface areas with a defined spatial elevation distribution (to represent e.g. ground surface or stratigraphic boundaries) and interconnecting the different layers. The model was divided into 5 layers comprising 6 slices (see Table 2). Varying boundary conditions and property distributions were assigned to the different layers. Layer 1 represents less permeable sediment near the northern domain boundary and parts of the aquifer of layer 2, 3 and 4. Layer 2, Layer 3 and Layer 4 represent an aquifer with high porosity and hydraulic conductivity. Layer 5 represents a part of the same aquifer with reduced hydraulic conductivity (-10%) and correspondingly reduced porosity. Stream infiltration data based on previous stream loss data using differential streamflow measurements were applied to slice 2. Horizontal drainage wells and, thus, water extraction are located in Slice 3.

Table 2. *Schematic structure division of layers and slices including their general geohydraulic function.*

Slice	Layer
Slice 1: top ground surface	
	Layer 1 Aquitard/Aquifer
Slice 2: clogging layer	
	Layer 2 Aquifer
Slice 3: horizontal drainage wells	
	Layer 3 Aquifer
Slice 4: monitoring wells	
	Layer 4 Aquifer
Slice 5	
	Layer 5 Aquifer with slightly reduced K and porosity
Slice 6: bottom of model area	

Porosity of the single layers has been determined by previous researchers, using tracer tests. Hydraulic conductivity of aquifer A varies between 1.5 x 10^{-2} m s^{-1} and 1.9 x 10^{-2} m s^{-1}, up to 5.5*10^{-2} m s^{-1} in the vicinity of the horizontal drainage wells, resulting in a high linear flow velocity of 60-70m d^{-1}. Further downstream, hydraulic conductivity approaches mean hydraulic conductivity again, varying between 1x 10^{-2} m s^{-1} and 3 x 10^{-2} m s^{-1} (Bichler et al., 2016). Figure 13 shows the hydraulic conductivity distributions for the different layers:

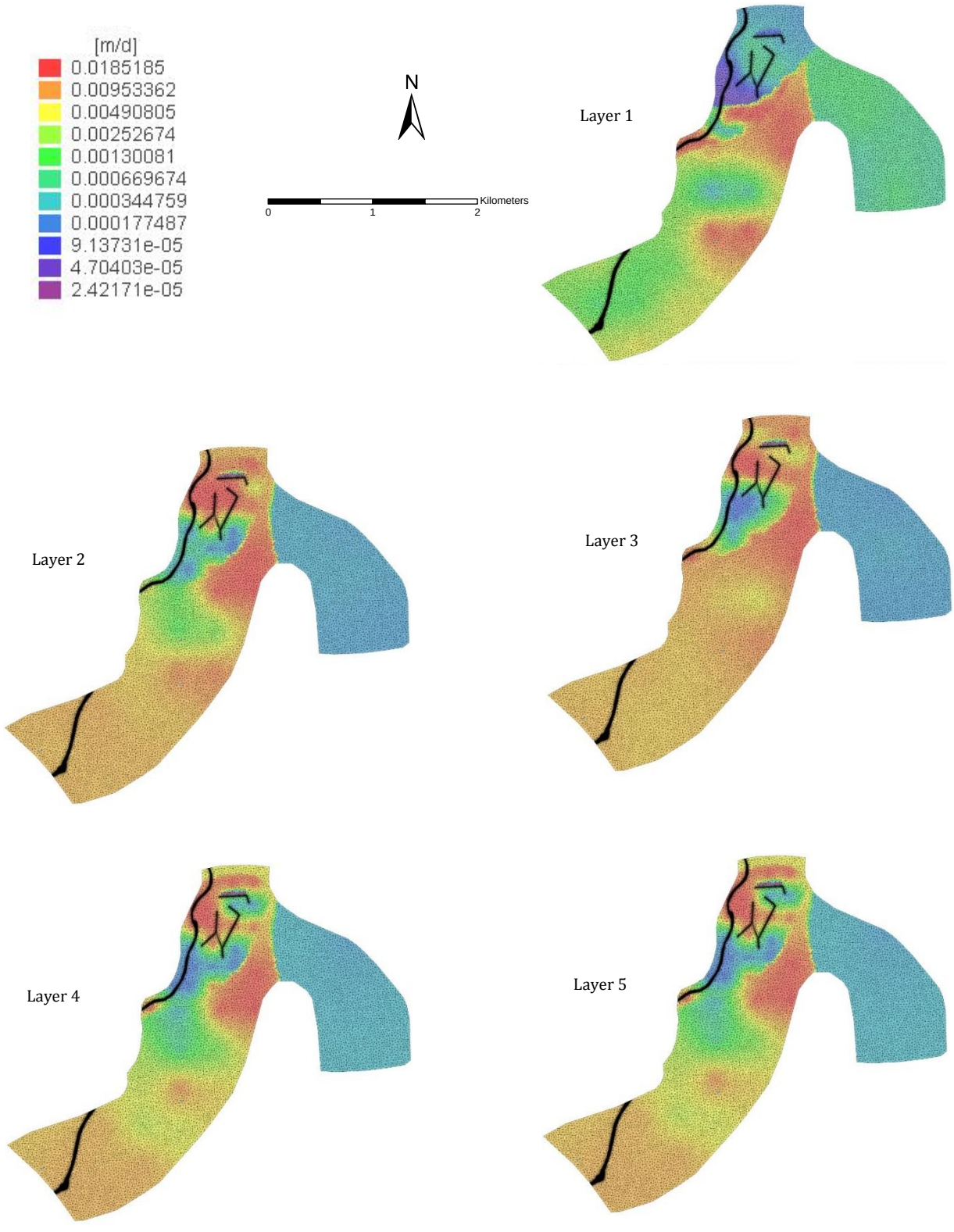

Figure 13. *The five layers and their respective hydraulic conductivity distribution. K ranges from 2.4·10^{-4} m s^{-1} to 9.2·10^{-2} m s^{-1}. Layer 2, 3 and 4 show the highest K values.*

Boundary and initial conditions

Initial conditions specify the value of the dependent variable at any point within a given model domain at a specific time. In geohydraulic models the hydraulic head, h, is used at the initial time $t = 0$. Based on hydraulic head data from observation wells, the initial hydraulic head was interpolated for the model domain.

Boundary conditions (BC) can either be constant, determined by static values, or time variant in transient simulations. In groundwater flow modelling three different boundary conditions are generally being distinguished:

- Dirichlet-type BC (1st order): specifies time-constant or time-varying values for the primary variable at a node or border segments (i.e. here hydraulic head)
- Neumann-type BC (2nd order): flux-type boundary condition that specifies the gradient of a scalar variable like in- or outflow (i.e. here water) at the element edges.
- Cauchy-type BC (3rd order): combination of Dirirchlet BC and Neumann BC. Specifies transfer properties between a reference value for the primary variable (e.g. hydraulic head) and groundwater (i.e. here leakage and/or infiltration of surface water into the aquifer).

(Bear and Cheng 2010; FEFLOW User Manual)

Inflow and outflow

Specified head boundary conditions (Dirichlet) at the considered point in time were applied to the south-western and the north-western part of the model area with a head difference of 25.1m and a gradient of 0.6275%. Groundwater abstraction rates were nodal applied in Slice 3 as a Neumann-type BC.

Infiltration and groundwater recharge

Discharge measurements were performed by earlier researchers to calculate flow difference of the partially infiltrating stream. The streambed was therefore divided into several reaches and the mean flow difference was evenly distributed within each reach, respectively, in the form of a Neumann BC. Thereof, stream loss per section was calculated using measured discharge rates (will be compared later). Impermeable tertiary bedrock was implemented as impermeable Neumann BC (no flow). Annual precipitation and evaporation data was obtained from national meteorological services and a mean groundwater recharge rate of 22.5 l s^{-1} km^{-2} was calculated by earlier researchers. Although some small amount of surface runoff into the stream is possible in the vicinity of the stream, water gain from

precipitation was assigned to the topmost layer as groundwater recharge, assuming no direct surface runoff.

Implementing EC_a-based streambed K_v estimates into the flow model

After pre-processing, interpolated EC_a values were linked to the nodes and elements, respectively, of the numerical model (using a Python programming interface) for visualisation, using the Transfer-Rate module in FEFLOW. The fluid in-transfer rate was calculated from Eq. 20 and assigned to the relevant elements in the streambed as Cauchy-type boundary condition:

$$\phi = \frac{K}{d} \qquad \text{(Eq. 20)}$$

where ϕ is the transfer rate, K is the hydraulic conductivity (i.e. processed electrical conductivity values) and d is the thickness of the clogging layer. Thickness of the clogging layer was assumed to be constant, in absence of borehole samples, and was set to d =1m.
Elevation data of the V-shaped stream profile was applied as Cauchy-type boundary condition to the nodes along the lines of the streambed raster-grid to represent the overlying water column and was set to steady state.

The Transfer-Rate module correctly displays the in-/and outflow conditions of the particular elements but cannot be used for water budget calculations, as it is designed for saturated conditions, where the formation of an unsaturated zone is excluded, thus overestimating the infiltration in deeper layers, leading to numerical instability. In addition, the occurrence of graphical artefacts is possible, as the extracted values from GIS apply solely to the element centres and are interpolated by FEFLOW towards the element edges.

Hence, the Fluid-Flux BC-module was used, where a pre-defined flux (Darcy flux), assuming a known gradient and a constant flux, is applied to the nodes along the stream line to correctly calculate infiltration rates. Eq. 20 was nodally assigned and elevation data of the stream profile was applied as Neumann-type BC. EC_a values were multiplied with 86400 to convert original units (m s^{-1}) to FEFLOW fluid-flux internal units (m d^{-1}).

Model adjustment

Three different models with default parameters were set up initially to compare infiltration rates with stream loss data.

In the initial model, EC_a data was assigned to streambed elements with altered values from a performed regression analysis. For the second and the third approach, value clusters were assumed. An EC_a cluster with corresponding fixed K_v-model was divided into two value ranges with $K_v=1\cdot10^{-5}$ m s^{-1} and $K_v=1\cdot10^{-7}$ m s^{-1} for EC_a<12 mS m^{-1} and EC_a >12 mS m^{-1}, respectively. These value ranges were chosen according to EC_a distribution in Figure 16, assuming the threshold value for the $\sigma' - K$ relationship to be EC_a<12 mS m^{-1}, where current flow is dominated by interconnected pore volume (i.e. σ_{el}) and EC_a>12 mS m^{-1}, where current flow is dominated by interconnected pore surface charge (σ'_{int}). Mean K_v-values were derived from reference literature (Domenico&Schwartz, 1998) and applied to the respective cluster. In an EC_a cluster with literature-assumed variable K_v distribution-approach, the model was further divided into three clusters with EC_a<12 mS m^{-1}, EC_a>12 and <20 mS m^{-1}, and EC_a >20 mS m^{-1}. Upper and lower thresholds/limits for each cluster are based on basic subsoil parameters, according to reference literature, which can be seen in Table 3 for selected soil configurations.

Table 3. *Subsoil configuration and respective kmin and kmax chosen for different ECa value-clusters. [1] Swiss Standard SN 670 010b, Characteristic Coefficients of soils, Association of Swiss Road and Traffic Engineers. [2] Domenico&Schwartz, 1998. Information obtained from: Geotechdata.info, Soil void ratio, http://geotechdata.info/parameter/permeability.html (as of October 7, 2013).*

Description	kmin [m s^{-1}]	kmax [m s^{-1}]	Cluster
Well graded sands, gravelly sands, with little or no fines [1]	$1\cdot10^{-8}$	$1\cdot10^{-6}$	1
Poorly graded sands, gravelly sands, with little or no fines [1]	$2.55\cdot10^{-5}$	$5.35\cdot10^{-4}$	1
Clayey gravels, clayey sandy gravels [1]	$5\cdot10^{-9}$	$5\cdot10^{-6}$	2
Marine clay [2]	$1\cdot10^{-13}$	$2\cdot10^{-9}$	3

The stream was further divided into 11 reach-domains, which can be seen in figure 14, according to classification by earlier researchers, for direct comparison of inferred infiltration rates and existing stream loss data. Individual inferred infiltration rates are presented in table 5 (Results).

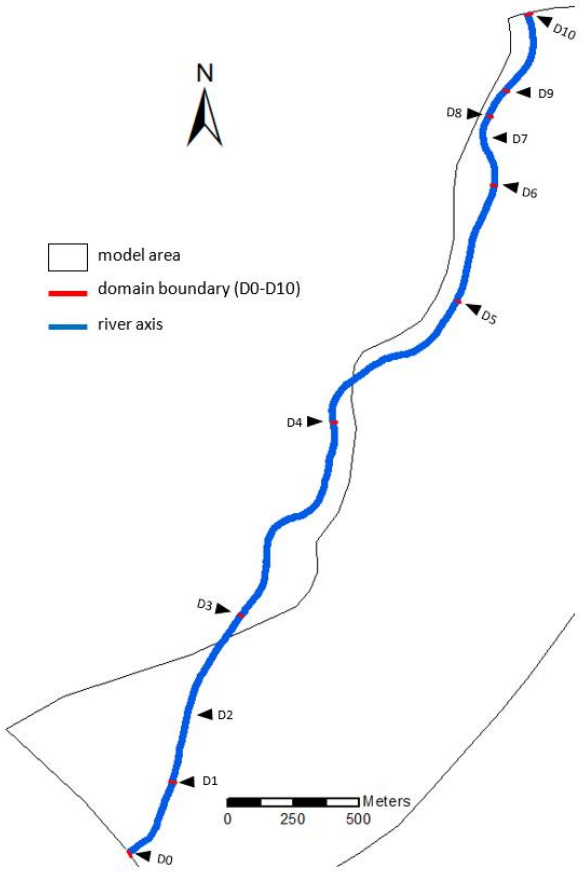

Figure 14. *Conceptual sketch of the stream partitioned in 11 domain reaches*

4. Results

4.1 Apparent electrical conductivity

Figure 15a and Figure 15b display the distribution of apparent electrical conductivity (EC_a), as measured with the CMD-2 and spatially interpolated using IDW, for the southern segment (upstream) and the northern segment (downstream) of the streambed, respectively, within the model area extent. Data was derived from three field campaigns conducted between June 2016 and September 2016 during low flow conditions.

The upstream fraction of the stream shows a minimum EC_a of 4.12 mS m^{-1} and a maximum of 23.08 mS m^{-1}, with a mean EC_a of 12.30 mS m^{-1}. Values near the weir at the southern border were derived from interpolated expansion of actual measured values 200 meters downstream. Allocation of ECa in this

area is therefore uniformly distributed and does not necessarily reflect true values but was derived using an approximation from the nearest measured mean values in the streambed. This also applies to the southern and northern borders of the downstream fraction.

In the downstream segment of the stream, EC_a ranges between a minimum of 1.29 mS m^{-1} and a maximum of 48.16 mS m^{-1}, with a mean EC_a of 10.17 mS m^{-1}. Relatively elevated values of >35 mS m^{-1} indicate high electrical conductivity which is supported by visual observations of impermeable tertiary clay bedrock cropping out, thus defining the southern stream border of the upstream part. Punctual areas of higher EC_a further downstream spatially correspond with artificially constructed breakwaters. 200m upstream the northern border a 150m long section showed relatively low EC_a of 1.5 to 3.5 mS m^{-1} with little to no variation. Stream morphology suggests that the streambed may potentially be underlain by concrete, which could, however, not be clearly verified by reference literature or other site information.

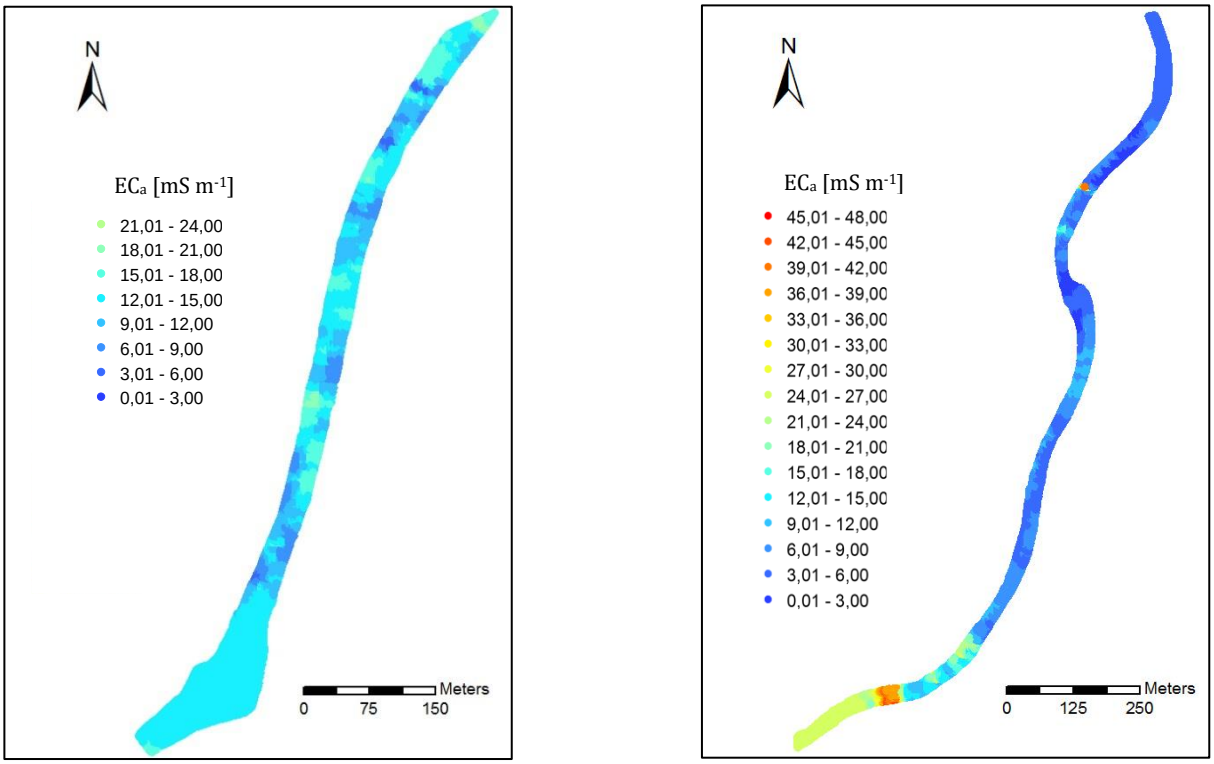

Figure 15. Upstream fraction of the streambed (left), downstream fraction of the streambed (right).

Figure 16 shows the statistical distribution of measured EC_a values. In total, 3890 points were measured. In a histogram with 5 mS m^{-1} data spacing, the 5-10 mS m^{-1} range accounts for the greatest proportion with 1691 measuring points (43.5%), followed by 10-15 mS m^{-1} and 0-5 mS m^{-1} with 1098 (28.2%) and 611 (15.7%) points, respectively. The remaining 487 points account for 12.5% of which 316 (8.1%) are attributable to 15-20 mS m^{-1}. Only 174 (4.4%) points range between 20-50 mS m^{-1} and are sparsely distributed around areas of small extent.

Figure 18 displays the EC_a distribution along the three measurement lines along the right side (x_00), the central axis (x_02) and the left side (x_04) of the streambed (orientation in streamflow direction). 1547 points were measured at x_02, 1576 points at x_00 and 767 points at x_04. Elevated stream flow velocities and water depths >1m impeded continuous walking in places, thus preventing equal point density along all three lines. EC_a distribution is comparable between the three lines, the greatest fraction of EC_a values ranging between 6-14 mS m^{-1} at x_00, 4-13 mS m^{-1} at x_02 and 6-16 mS m^{-1} at x_04. This is by and large consistent with the total distribution of EC_a indicated in Figure 16.

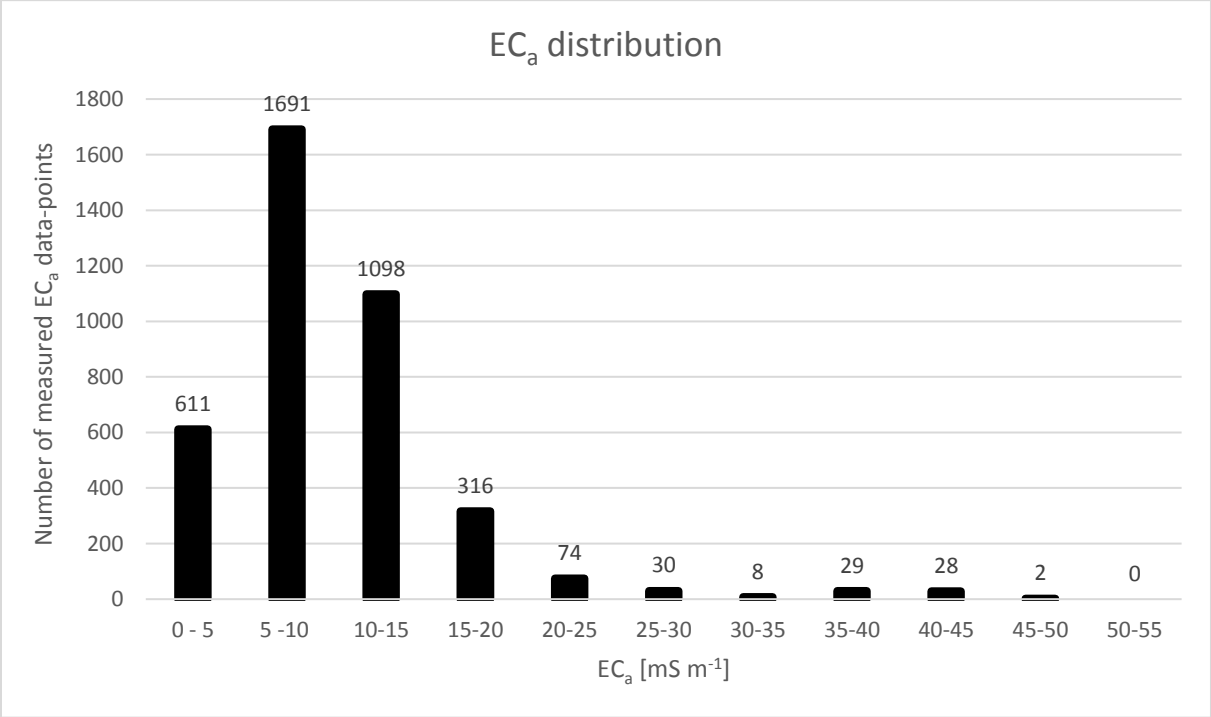

Figure 16. *Histogram of the statistical distribution of measured EC_a points*

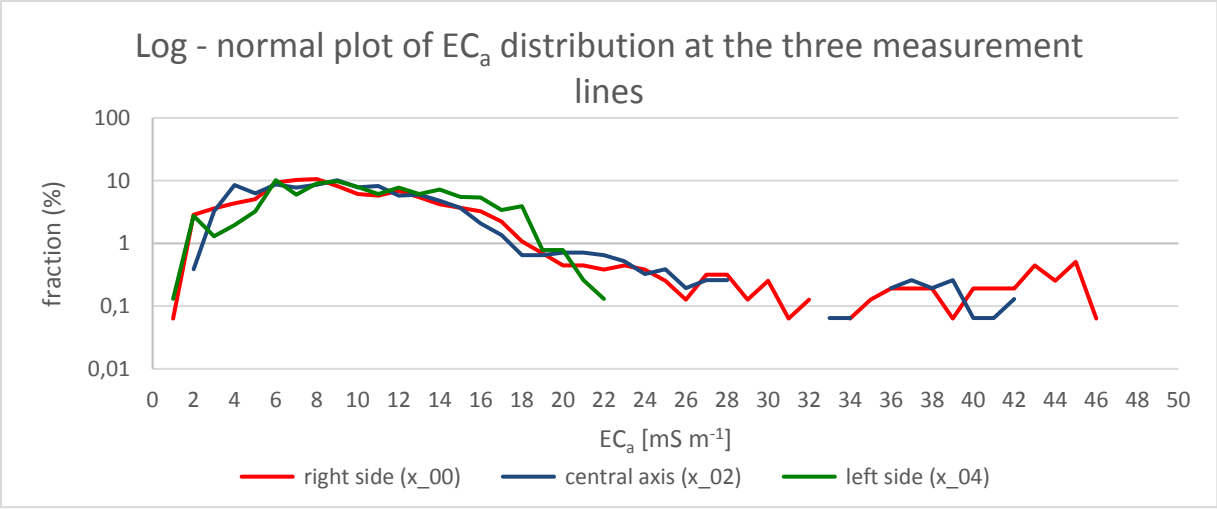

Figure 17. *Distribution of measured EC_a along the right side (x_00), the central axis (x_02) and the left side (x_04) of the streambed.*

Figure 18a and Figure 18b depict EC_a against streambed distance from upstreammost model extent, as point data derived along the three measurement lines x_00, x_02 and x_04.

Figure 18a displays the stream section of 0-1200m with EC_a values ranging from 6.02-18.60 mS m^{-1} at line x_00, 6.89-20.31 mS m^{-1} at line x_02 and 4.12-23.08 mS m^{-1} at line x_04. In figure 18b the stream section of 2200-3600m is shown, EC_a values at x_00 ranging from 0.78-45.36 mS m^{-1}, 1.43-41.62 mS m^{-1} at line x_02 and 0.99-20.77 mS m^{-1} at line x_04. Vertical grey lines indicate natural or anthropogenic barriers made from concrete, boulders, wood or metal, integrated into the streambed (taken with a handheld GPS system with an uncertainty of ± 10m). Vertical red lines mark the approximated position of the impermeable tertiary bedrock.

EC_a values in figure 18a often display peaks upstream or at and troughs downstream of natural (e.g. beaver dam) and anthropogenic (e.g. spur dikes, bottom steps) barriers in the streambed. This is not fully consistent for data along all three lines at every barrier but every line eventually displays peaks at individual barriers. Both, natural and anthropogenic barriers, may enable upstream deposition of fine grained material due to reduced flow velocities, thus leading to higher EC_a values (>15mS m^{-1}) and lower infiltration rates in this particular area. After the barriers, EC_a decreases with troughs often showing higher average EC_a values than the baseline before the peaks/barriers. The decrease in EC_a shortly after the barriers could be the result of decreased sedimentation of fine grained sediment material, due to higher flow velocities, leading to increased stream-aquifer exchange flow through the sediment material.

These findings are not consistent with anthropogenic barriers, which may presumably involve metal and/or concrete in their construction (i.e. flow constructions and bottom steps) in figure 18b. Downstream these constructions pool-like structures formed, leading to reduced flow velocities, which may have given a more pronounced rise to the deposition of fine grained sediments and resulting in increased EC_a after the barriers. Conceptually, as the bottom steps are constructed from concrete, several meters upstream of them, they would inhibit upstream infiltration, in line with relatively continuously low EC_a values (<10 mS m^{-1}). The outlier to this at 3500m in figure 18b is consistent with an undocumented (metallic) observation well in the streambed, encountered during measuring, leading to occasionally high EC_a values up to 59.63 mS m^{-1}. In figure 18a, peaks in EC_a can be seen between several barriers, at each line. They may represent unknown built-in artificial. Elevated EC_a values up to 27.70 mS m^{-1} were measured between several spur dikes, which were installed on the right side of the stream between 2400 and 2500m (Figure 18b). This is in line with pool formation between the dikes. The dikes promote larger flow velocity contrasts in the streambed, resulting in the formation of pools with little to no flow in the downstream area, immediately after the dikes, but also resulting in smaller high-flow velocity segments in the cross-sectional flow velocity distribution. The

reduced flow velocity would, conceptually, aid in the sedimentation of fine grained particles in the pool, which in turn, again, may result in decreased infiltration rates and elevated EC_a values.

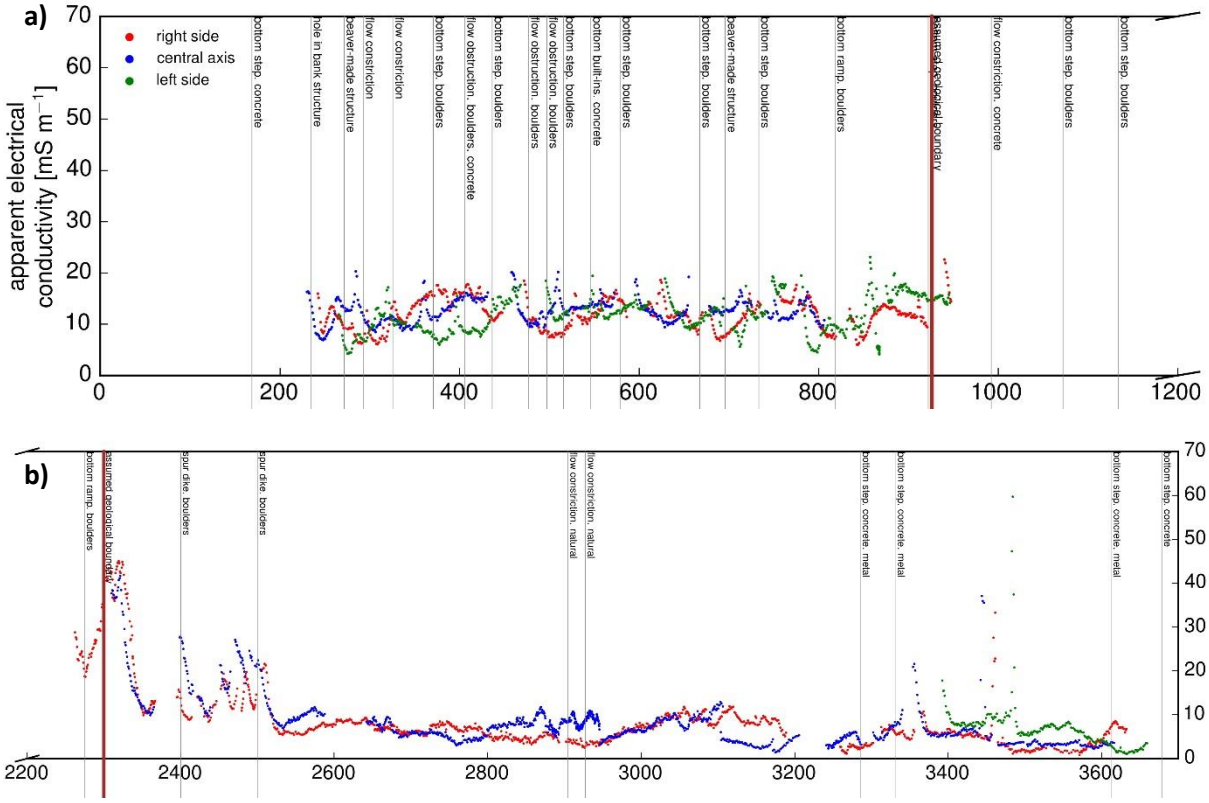

Figure 18. *Apparent electrical conductivity plotted against streambed distance from upstreammost model extent. 0 – 1200m (a); 2200 – 3600m (b).*

4.2 Hydraulic conductivity

Table 4 includes measured K_v values, which were collected using open-bottom infiltrometers, during field trips conducted between September 2016 and May 2017 and corresponding EC_a values, derived from IDW-interpolated EC_a data at the closest location to the respective infiltrometer positions. In total, 49 infiltrometer measurements were performed within three sections of the streambed. Of these 49 measurements, 45 are listed in Table 4. Four values were ignored due to their magnitude close to $1 \cdot 10^{-1}$ m s^{-1}, suggesting sediment column disturbance, potentially by cobbles or coarse gravels, hindering representative sediment capturing within the infiltrometer, leading to largely overestimated K_v values. The remaining 45 streambed K_v values range between $1.05 \cdot 10^{-3}$ m s^{-1} and $5.13 \cdot 10^{-7}$ m s^{-1}, mean K_v was found to be $1.90 \cdot 10^{-3}$ m s^{-1}. Histograms in figure 19 suggest that neither K_v nor $\log_{10}K_v$ is normally distributed.

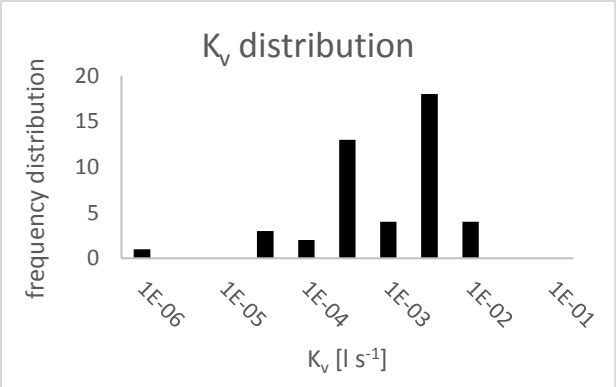

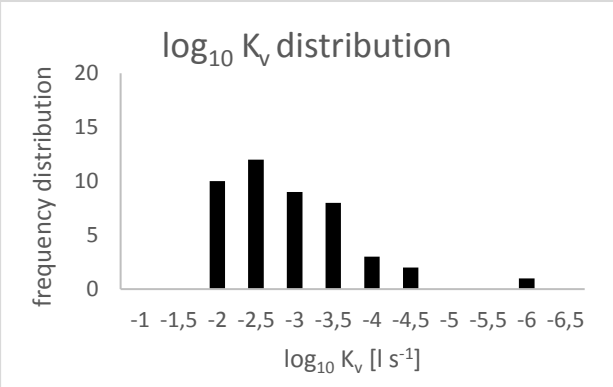

Figure 19. Distribution of streambed K_v (left), log_{10} distribution of streambed K_v (right)

Table 4. *Hydraulic conductivities and corresponding apparent electrical conductivity grouped according to three spatial measurement sections.*

Section 1			Section 2			Section 3		
ID	K_v [m s^{-1}]	EC_a [mS m^{-1}]	ID	K_v [m s^{-1}]	EC_a [mS m^{-1}]	ID	K_v [m s^{-1}]	EC_a [mS m^{-1}]
Inf-01	$2.75 \cdot 10^{-3}$	5.44	Inf-23	$8.90 \cdot 10^{-4}$	25.92	Inf-32	$1.70 \cdot 10^{-3}$	4.94
Inf-02	$1.09 \cdot 10^{-3}$	6.67	Inf-24	$1.28 \cdot 10^{-4}$	23.72	Inf-33	$1.60 \cdot 10^{-4}$	4.51
Inf-03	$1.70 \cdot 10^{-3}$	6.40	Inf-25	$5.13 \cdot 10^{-7}$	20.72	Inf-34	$4.80 \cdot 10^{-3}$	5.18
Inf-04	$6.34 \cdot 10^{-3}$	6.26	Inf-26	$2.62 \cdot 10^{-4}$	20.02	Inf-35	$5.50 \cdot 10^{-4}$	5.12
Inf-05	$2.38 \cdot 10^{-4}$	6.65	Inf-27	$4.64 \cdot 10^{-3}$	26.72	Inf-36	$1.80 \cdot 10^{-3}$	4.96
Inf-06	$5.74 \cdot 10^{-3}$	6.94	Inf-28	$8.20 \cdot 10^{-3}$	20.42	Inf-37	$5.00 \cdot 10^{-4}$	5.51
Inf-07	$3.55 \cdot 10^{-5}$	6.04	Inf-29	$1.36 \cdot 10^{-4}$	15.62	Inf-38	$1.00 \cdot 10^{-4}$	6.09
Inf-08	$4.75 \cdot 10^{-4}$	7.00	Inf-30	$9.92 \cdot 10^{-4}$	21.31	Inf-39	$2.20 \cdot 10^{-3}$	5.82
Inf-09	$3.26 \cdot 10^{-2}$	7.00	Inf-31	$4.45 \cdot 10^{-4}$	21.72	Inf-40	$1.70 \cdot 10^{-3}$	6.10
Inf-10	$2.84 \cdot 10^{-3}$	9.06				Inf-41	$2.60 \cdot 10^{-4}$	6.00
Inf-11	$1.02 \cdot 10^{-4}$	10.32				Inf-42	$4.20 \cdot 10^{-3}$	2.74
Inf-12	$2.97 \cdot 10^{-4}$	8.24				Inf-43	$3.70 \cdot 10^{-4}$	2.88
Inf-13	$8.31 \cdot 10^{-5}$	6.89				Inf-44	$2.70 \cdot 10^{-3}$	4.14
Inf-14	$3.67 \cdot 10^{-3}$	7.08				Inf-45	$3.40 \cdot 10^{-4}$	3.33
Inf-15	$4.81 \cdot 10^{-3}$	8.30						
Inf-16	$1.14 \cdot 10^{-3}$	8.46						
Inf-17	$4.61 \cdot 10^{-3}$	4.54						
Inf-18	$3.22 \cdot 10^{-2}$	5.14						
Inf-19	$1.05 \cdot 10^{-3}$	5.30						
Inf-20	$3.45 \cdot 10^{-2}$	8.00						
Inf-21	$7.94 \cdot 10^{-3}$	5.79						
Inf-22	$2.66 \cdot 10^{-3}$	5.24						

Figure20a, Figure20b and Figure20c plot the hydraulic conductivity against the apparent electrical conductivity at the respective infiltrometer positions for section 1, section 2 and section 3, respectively. Figure19a and Figure19c show a very weak positive linear-$\log_{10}$ correlation of EC_a-K_v with a coefficient of determination (R^2) of 0.0773 (a) and 0.2146 (c), Figure19b shows a very weak negative linear-$\log_{10}$ correlation with R^2 of 0.0948, as well.

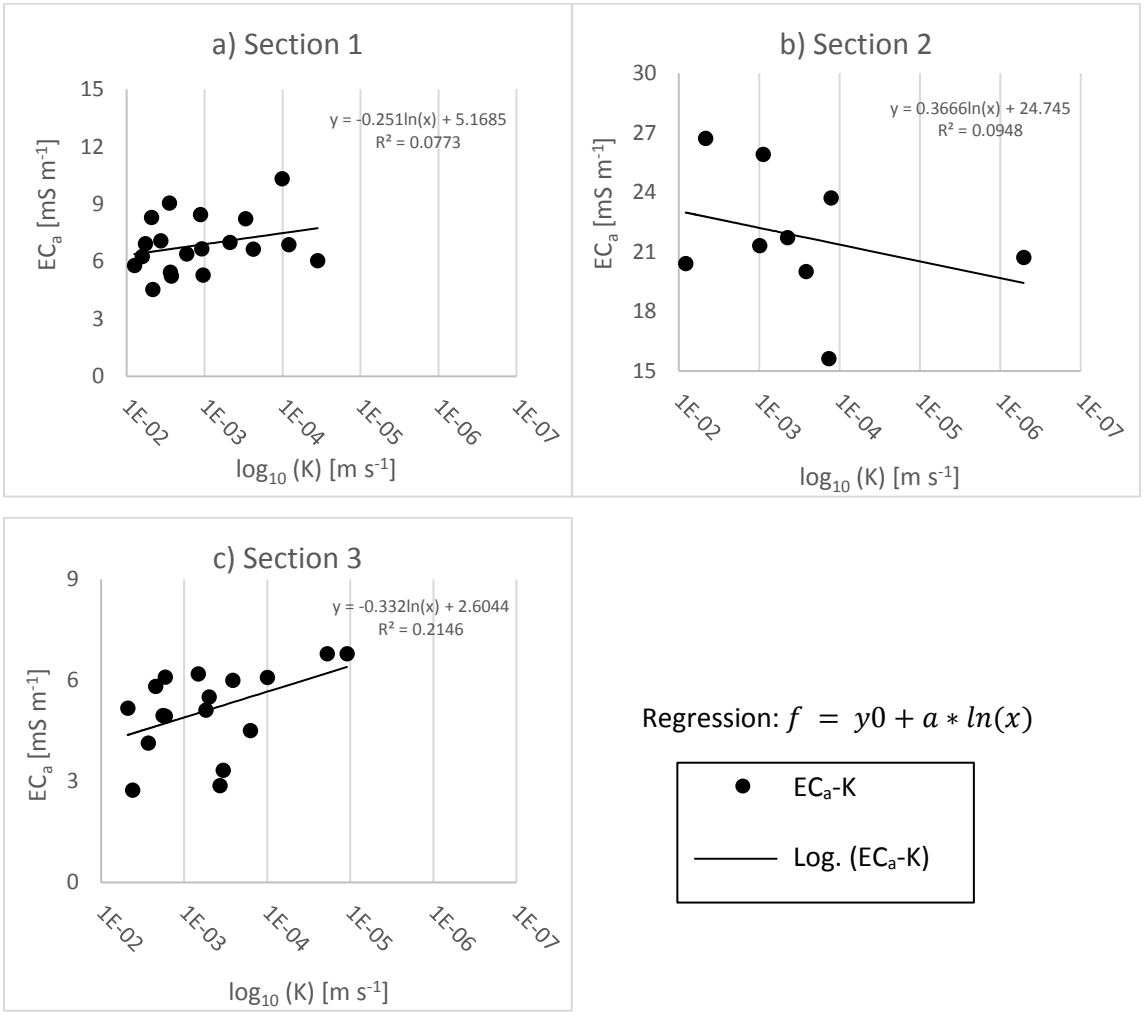

Figure 20. *Hydraulic conductivity plotted against apparent electrical conductivity at the co-located infiltrometer coordinates for section 1 (a), section 2 (b) and section 3 (c), respectively. Regression formula coefficients are indicated, as well as trend line and coefficient of determination (R^2).*

Figure21a displays the hydraulic conductivity, measured in all three sections, against the closest apparent electrical conductivity at the respective infiltrometer positions. Figure 21b plots K_v against EC_a<12 mS m^{-1}. Figure 21c plots K_v against EC_a>12 mS m^{-1}. These value ranges were chosen according to a pre-defined setup (see chapter Model adjustment). Trend lines show a very weak positive linear-

$\log_{10}$ EC_a-K_v correlation for figure 21a and figure 21b and a very weak negative linear-$\log_{10}$ EC_a-K_v correlation for figure 21c.

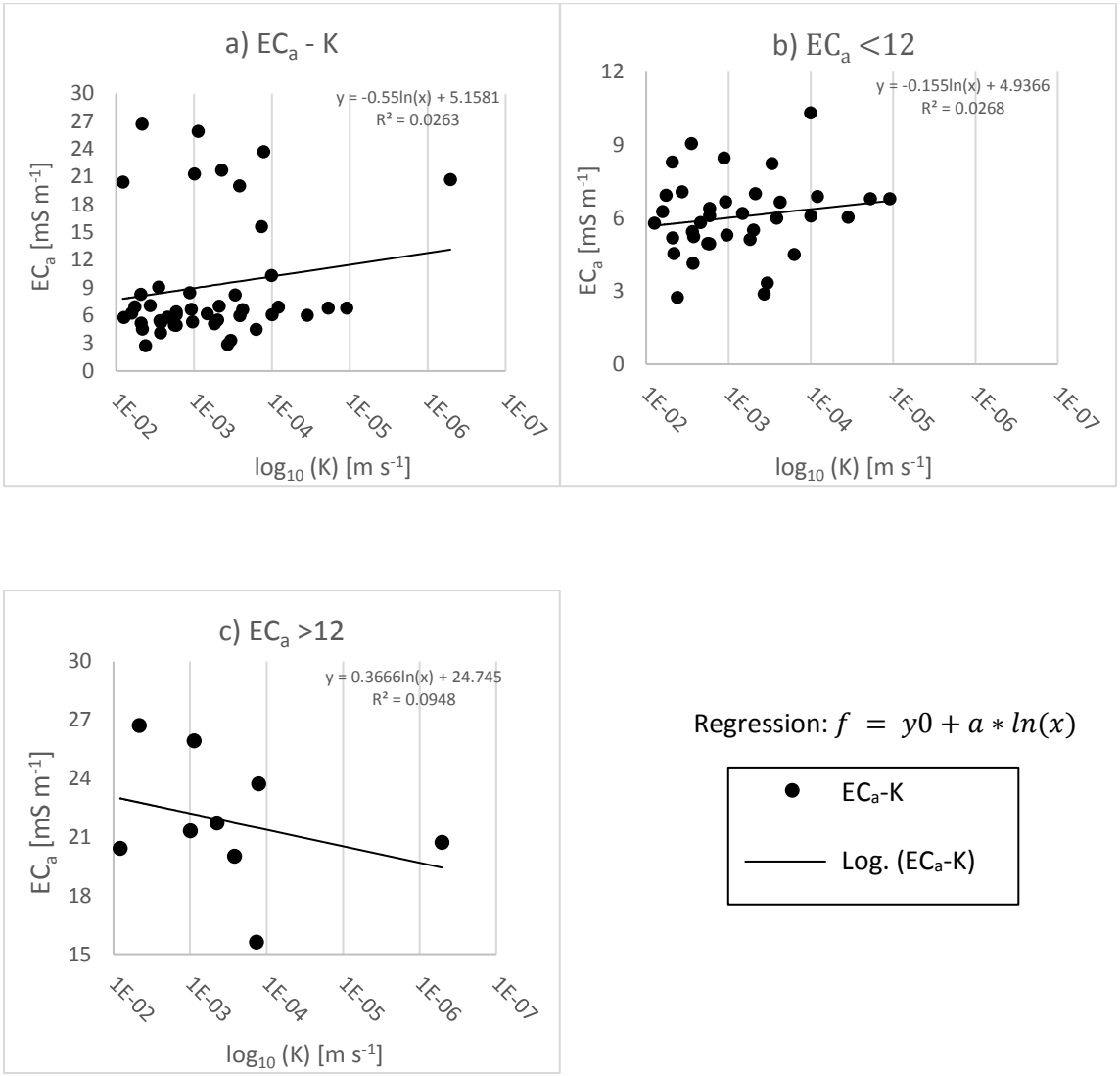

Figure 21. *Total number of measured K_v plotted against EC_a at respective infiltrometer positions (a). EC_a values smaller than 12 mS m^{-1} (b); EC_a greater than 12 mS m^{-1} (c). Regression formula and regression coefficients are indicated, as well as coefficient of determination (R^2).*

4.3 Infiltration rate

The state of research and common research theory show an inversely proportional relationship for EC_a-K_v, compared to the results in Fig. 21a, Fig. 21b and Fig. 21c. Considering the weak coefficient of determination and the calculated water budget results shown in table 5, a literature based approach was chosen to link apparent electrical conductivity and hydraulic conductivity.

Table 5 lists previously measured low flow infiltration rates and compares them with inferred infiltration rates using different EC_a-K_v relationships in the implementation as a Cauchy-type boundary condition (see methods). Positive values indicate stream infiltration, negative values indicate feeding fluxes to the stream. Column 1 lists the respective 11 domains (D0-D10), as indicated by the infiltration measurements. Column 2 lists the measured stream loss rates. An uncertainty error of 4.04% was specified by earlier researchers for the conducted measurements. Infiltration rates, with stream loss rates within the measurement uncertainty of ≤ ±35l s^{-1} were ignored. Domains D0 and D10 were implemented during the present workflow to complete the outline of the streambed at the northern and southern border of the model area and were therefore not compared.

Column 3 shows the results for an EC_a-K_v regression-based infiltration rate model with calculated hydraulic conductivity, according to the regression formula in figure 21a. Infiltration of both total and domain specific values are underestimated by several orders of magnitude, resulting in a low total infiltration of 2.374 l s^{-1}. Due to this divergence and the weak correlation between EC_a and K_v, K values were adjusted according to reference literature (Domenico&Schwartz 1998) and several attempts to find the best-fitting threshold parameters were performed.

Initially, a model with two fixed value clusters was constructed to evaluate the effect of choosing upper and lower K_v limits for the clusters. More precisely, EC_a<12 mS m^{-1} was set to K=1·10^{-5} m s^{-1} and EC_a>12 mS m^{-1} was set to K=1·10^{-7} m s^{-1}. Total infiltration was calculated to be 2.378 l s^{-1}, displaying relatively low infiltration results for all 11 domains. The threshold for the fine grained dominated part (EC_a>12 mS m^{-1}) was subdivided into two clusters to accurately represent realistic conditions found in standard sediment configurations. Approximating the present aquifer system conditions, with a mean hydraulic conductivity of 1.5·10^{-3} m s^{-1}, three value ranges were defined, based on table 3, with fixed minimum (kmin) and maximum (kmax) threshold values for K. For the first value-cluster EC_a<12 mS m^{-1}, kmin= 1·10^{-8} m s^{-1} and kmax= 5.35·10^{-5} m s^{-1} were selected, representing the lower limit for well graded sands/gravelly sands (kmin) and the upper limit for poorly graded sands/gravelly sands with little or no fines (kmax). For EC_a >12 and <20 mS m^{-1} clayey gravel/clayey sandy gravel was chosen with the limits kmin= 5·10^{-9} m s^{-1} and kmax= 5·10^{-6} m s^{-1}. The third value-cluster, EC_a>20 mS m^{-1} was set to kmin= 1·10^{-13} m s^{-1} and kmax= 2·10^{-9} m s^{-1}, representing compacted clay. A total infiltration rate of 2.94 l s^{-1} was calculated for the EC_a cluster with literature-assumed variable K_v distribution, still underestimating measured stream loss values by two orders of magnitude.

As Figure 16 demonstrated, 95.5% of all measured values do not exceed 20 mS m^{-1}. Of this 95.5%, 72.5% range between 0 and 12 mS m^{-1}. Thus, particular emphasis was placed on adjusting the EC_a <12 mS m^{-1} cluster, as changes in this value-range presumably would have the greatest impact on the groundwater flow model. Therefore, threshold values for the first cluster were adjusted within a given range, the second and the third EC_a-cluster were not modified.

To assess whether kmin or kmax of the cluster had the greater impact on the inferred infiltration rate, different threshold values were tested. The uppermost limit for kmax was set to $1 \cdot 10^{-3}$ m s^{-1}, the lowest limit for kmin was found to be within the range of $1 \cdot 10^{-5}$ m s^{-1} and $1 \cdot 10^{-6}$ m s^{-1}. For the EC_a<12 mS m^{-1} cluster a set kmax=$1 \cdot 10^{-3}$ m s^{-1} and kmin=$5 \cdot 10^{-6}$ m s^{-1}, an infiltration in domains D1-D9 of 430.34l s^{-1} and a total infiltration of 570.01l s^{-1} was estimated.

Results for the EC_a cluster with fixed kmax and calculated kmin-model show an infiltration rate of 467.25l s^{-1} in domains D1-D9 and a total infiltration of 617.90l s^{-1}. Compared to the measured stream loss, the total infiltration rate for D1-D9 is approximately equal, only overestimated by 1.25l s^{-1} (0.26%). Infiltration rates for D8-D10 lie within the ≤ ±35 l s^{-1} measurement deviation, expressed by earlier researchers. Domains D0, D2 and D4 exceed the measurement deviation, with domain D0 displaying the highest overall infiltration rate of 123.62 l s^{-1}. Infiltration rates in domain D1 and D3 are unequal to measured stream loss rates but show consistently high comparable results, compared to the other domains.

Table 5. *Measured stream loss rates compared to inferred infiltration rates, for different approaches.*

Inferred infiltration rates compared to stream loss data [l s^{-1}]						
Domain	Stream loss data from discharge measurements	EC_a cluster with fixed kmax and calculated kmin	EC_a-K_v regression-based infiltration rate	EC_a cluster with corresponding fixed K_v	EC_a cluster with literature-derived variable K_v distribution	EC_a cluster with assumed variable kmin and fixed kmax
D0	0	123.624	2.794	2.7959	2.907	114.639
D1	127	99.198	-0.005	$-1.437 \cdot 10^{-3}$	0.088	90.740
D2	0	79.626	0.0021	$3.558 \cdot 10^{-3}$	0.076	72.911
D3	270	113.556	$-9 \cdot 10^{-4}$	$-2.689 \cdot 10^{-3}$	0.101	103.917
D4	0	50.268	$5.85 \cdot 10^{-5}$	$1.319 \cdot 10^{-4}$	0.047	46.618
D5	104	21.549	$-1.40 \cdot 10^{-4}$	$2.690 \cdot 10^{-5}$	0.019	19.859
D6	-110	37.187	$5.04 \cdot 10^{-4}$	$5.354 \cdot 10^{-5}$	0.035	34.862
D7	75	7.740	$1.4 \cdot 10^{-4}$	$7.886 \cdot 10^{-5}$	0.006	7.151
D8	0	25.038	$4.6 \cdot 10^{-4}$	$-4.508 \cdot 10^{-4}$	0.023	23.259
D9	0	33.084	-0.0011	$-1.542 \cdot 10^{-3}$	0.030	31.018
D10	0	27.032	-0.415	-0,415	-0.389	25.032
Total	466	617.908	2.374	2.378	2.948	570.012
D1 - D9	466	467.251	-0.004	$-2.27 \cdot 10^{-3}$	0.429	430.340

5. Discussion & Conclusion

This thesis examined whether or not apparent electrical conductivity (EC_a) data, using electromagnetic induction measurements (EMI), can be linked to reach-scale streambed vertical hydraulic conductivity (K_v) of a losing-disconnected streambed at a bank filtration site. EMI-supported derivation of a Cauchy-type boundary condition along the streambed in an existing groundwater flow model were compared to stream loss data from previous discharge measurements.

Apparent electrical conductivity EC_a

Recent research almost exclusively relates to EC_a-derived properties of the shallow subsurface on dry ground surfaces. Only little research has been conducted on EC_a distribution within alluvial streambeds. The general magnitude of measured streambed apparent electrical conductivity (EC_a) values correspond well with values investigated by other researchers. Binley et al. (2013) found EC_a to vary between 10 mS m^{-1} and 35 mS m^{-1} within a 200m transect at a gaining stream in North Scotland, comprising mainly loose gravel alluvium overlying unconsolidated sandstone bedrock. Hruby (2016, unpublished) found EC_a to vary between 7 mS m^{-1} and 20 mS m^{-1} within a 100m transect at a stream in Nebraska comprising several meters of alluvial gravelly sands (Brice, J. C., 1964). They measured a mean EC_a of 13.03 mS m^{-1}, corresponding well to the mean EC_a at the present site (mean EC_a upstream=12.30 mS m^{-1}, downstream=10.14 mS m^{-1}), and relatively comparable statistical distribution of EC_a, with the 10-14 mS m^{-1} range accounting for the greatest proportion.

Peaks of EC_a close to the natural and anthropogenic barriers, built without concrete or metal, may potentially correspond with locally reduced flow velocities upstream of these barriers, resulting in the sedimentation of fine grained material (silt and clay). Genereux et al. (2008) found small differences between upstream and downstream reaches of a temporarily existing beaver dam, with mean upstream streambed K being reduced by 23%, potentially caused by upstream settling of fine particles. This probably does not apply to the barriers constructed or enhanced with concrete, as they may provide sealing anyway. With a saturated hydraulic conductivity (K_s) of concrete being around $5.87 \cdot 10^{-14}$ m s^{-1} (Schneider et al. 2012) it is practically impermeable, and therefore expected to result in low EC_a values, as displayed in Fig. 18b at the barriers at 3300m. Due to the relatively frequent regulations of the stream course and shallow water depths, between 3400m and 3650m in Fig. 18, low ECa <9 mS m^{-1} correspondingly suggest low hydraulic conductivity caused by extensive concrete built-ins.

Streambed vertical hydraulic conductivity K_v

Streambed hydraulic conductivity can be spatially highly variable and was found to vary by over 3 orders of magnitude within a few meters, at the present investigation site. Genereux et. al (2008) found K to vary over 4 orders of magnitude within a 262m long river transect while Datry et al. (2014) found K to vary over 3 orders of magnitude, as a result of 2463 point measurements of falling head slug tests in more than 100 stream reaches. Spatial distribution of streambed K_v at the test site was found to be not normally distributed (see Fig. 19). This is consistent with results observed by other researchers (e.g. Springer et al., 1999, Chen, 2005, Genereux et al., 2008). Deposition and grading of unconsolidated material in the streambed may result in strong heterogeneities and directional trends in K_v direction.

Although K_v was found to be 2-10 times higher in the centre of the stream channel ($1.18 \cdot 10^{-3}$ -$2.30 \cdot 10^{-3}$ m s^{-1}) , compared to the sides ($2.44 \cdot 10^{-3}$ -$2.37 \cdot 10^{-4}$ m s^{-1}) , EC_a data does not support this observation: EC_a values >17 mS m^{-1} were measured in section 2 (mean K=$1.18 \cdot 10^{-3}$ m s^{-1}) , which we assume to be σ'_{int}-dominated, expecting a negative logK_v -log EC_a relationship and thus, low K_v values. In section 3 (mean K=$1.30 \cdot 10^{-3}$ m s^{-1}) EC_a values <6 mS m^{-1} were measured, which we assume to be σ_{el}-dominated, expecting a positive logK_v -log EC_a relationship and thus, lower K_v values for EC_a<6 mS m^{-1}, as well. No explicit distinction was made between the sides and the centre of the channel while measuring K_v during the field campaign, also the low density of K_v data (n=45) suggests that these results are not statistically significant. Besides the 4 measurement values that were ignored due to their magnitude close to $1 \cdot 10^{-1}$ m s^{-1}, potentially caused by sediment column disturbance, additional point measurements with high K_v values would potentially have to be excluded for the same reason. After repeated use, the open-bottom pipes were noticeably severely deformed at the bottom-end, probably due to impact damage after hitting cobbles or coarse gravels, potentially changing the sediment architecture which may have led to distorted results. Piezometers with a filter screen and closed ends for point K_v measurements allow for vertical outflow near the bottom, minimizing the potential effects on sediment architecture. They would pose a promising and low cost alternative for coarse grained streambeds and are already widely used (e.g. Datry *et al.,* 2014; Baxter *et al.,* 2003).

EC_a-K_v relationship

As K_v values only show a weak relation to adjacent EC_a measurements in figure 21a, figure 21b and figure 21c, with results inversely proportional to the current state of research, overestimation of point K_v measurements may have had a significant impact on the regression analysis, resulting in weak coefficients of determination (R^2=0.0263 for EC_a<12 mS m^{-1} and R^2=0.0948 for EC_a>12 mS m^{-1}). As for figure 21a and figure 21b, lower K_v values could have shifted the slope of the trend lines towards a

positive linear $\log K_v$-EC_a relationship. Figure 21c shows a positive correlation, where high K_v values $>1 \cdot 10^{-3}$ m s^{-1} may have been overestimated as well.

Comparative values are scarce. Little to no research was conducted to link EC_a and K_v at the streamreach-scale, using EMI methods: Brosten et al. (2011) compared $\ln(EC_a)$ and $\ln(K)$ for 10 observation wells, using a multi-frequency EM-meter. They found a weak relation for all frequencies with correlation coefficients ranging from 0.21 to 0.14, being equal to R^2=0.0441 and R^2=0.0196. Such poor correlation could also result from discrepancies between the measurement support volumes of the EMI sensor and the infiltrometer. Compared to the diameter of the coils in the CMD-2 (r=1.89m), the performed K_v measurements only represent the vertical hydraulic conductivity of the comparatively small volume of captured streambed sediment within the infiltrometer pipes (r=4cm). EMI sensors with smaller coil separations exist (e.g. CMD-Mini Explorer with r=32cm), but, on the other hand, reducing coil spacing could decrease depth of exploration and, therefore, measurements could be too shallow to capture the full vertical extent of a streambeds´ clogging layer. Another potential error could arise from vertical layering of the streambed sediments. The highest sensitivity of the CMD-2 is within the first 50cm, with respect to the stream bottom. The fact of sensitivity being a function of depth in combination can lead to slightly variable EC_a values for similarly grained clogging layer material with varying thicknesses as well as for similarly thick clogging layer material with varying grain size distribution or compaction. Hendrickx et al. (2002) obtained a soil conductivity profile with an EMI sensor held at several heights above the ground surface. However, multiple depth measurements require the set-up of multi-layered conceptual models and time consuming inverse modelling. The practical and rapid application of such approaches is therefore limited. Multi-frequency EMI instruments and multi-coil EMI sensors, with multiple coil spacings, can cover multiple depths with a single measurement, as well. The application of multi-frequency sensors requires, again, more extensive inverse modelling efforts. The prediction of K_v is limited by the fact, that the relative contribution of electrical conductance from the pore volume pathway and from the pore surface area pathway to EC_a cannot be inferred, using EMI methods (Slater, 2007). Induced polarization (IP) additionally records the electrical charge storage, associated to interface polarization. It´s measurable magnitude can be linked to geometrical characteristics of the pore space and, as a result, the relative contribution to EC_a can be computed.

Additional grain size analysis from streambed sediment cores could help to characterize streambed grain size distribution, to estimate hydraulic conductivity and clogging layer thickness, as well as for outlier detection in order to distinguish between sediment with naturally relatively high K_v and K data with overestimated K_v, due to sediment architecture disturbance while installing the open-bottom pipes. In order to keep the stream-aquifer exchange rates at the site unaffected, invasive methods, such as sediment coring, was refrained from.

Considering the low number of point K_v measurements and the lack of sediment core samples, there is lack of supporting information to check the point measurements for effects of the potential numerous measurement errors, as previously described.

Infiltration model

Considering the weak EC_a-K_v correlation from regression analysis (Fig. 21a), deviations in infiltration rates compared to previous stream loss measurements were expected for the EC_a-K regression-based infiltration rate-model. To investigate the resulting infiltration rates using upper and lower limits for K_v, derived from reference literature (Domenico&Schwartz, 1998), using mean values for gravelly sand and fine sand, an EC_a cluster with corresponding fixed K-model (EC_a<12 mS m^{-1}, K=1·10^{-5} m s^{-1} and EC_a>12 mS m^{-1}, K=1·10^{-7} m s^{-1}) was chosen. Infiltration rates were underestimated by several orders of magnitude, with fixed K_v values of 1·10^{-5} m s^{-1} for EC_a<12 mS m^{-1}, the EC_a cluster having the greatest influence. During adjustment and further narrowing of EC_a cluster with literature-derived variable K_v limits (see Table 3), it was found, that the total infiltration rate was more sensitive to the upper limit (kmax) than the lower limit (kmin). A kmax of 1·10^{-3} m s^{-1} was observed to be the highest upper limit without encountering numerical instabilities. The best-fitting model, comprising EC_a cluster with fixed kmax and calculated kmin, was adjusted to corresponding infiltration rates for domains D0-D9. The computed upper limit of kmin= 2.18·10^{-5} m s^{-1} matches with measured streambed K_v limits, not exceeding 8.31·10^{-5} m s^{-1} (considering section 1 and section 3, not considering Inf-25 in section2, a possible outlier). Inferred individual domain infiltration rates differ from stream loss measurements by several tens of l s^{-1}, although showing a corresponding trend in reach-scale infiltration. Original stream loss measurements already show an uncertainty of ± 35l s^{-1}, which could have been enhanced due to numerical errors during the computation. Domain D0 displayed the highest infiltration rates, which could not be compared, as no stream loss data exists for this reach. Additional stream loss measurements in domains D0 and D10 would be necessary to confirm inferred infiltration rates.

Conclusion

Electromagnetic induction measurements are well suited for collecting large amounts of electrical data of the shallow subsurface but seem to lack potential in investigating infiltration rates through a possible clogging layer within a streambed, with the proposed setup. Whether current flow is dominated by interconnected pore volume or interconnected surface charge is highly site-specific and difficult to be inferred without the collection of sediment core samples. Even with existing core samples, extensive measurements of hydraulic conductivity have to be conducted to relate apparent

electrical conductivity to hydraulic conductivity at the reach-scale. The very weak EC_a-K_v correlation is partially consistent with some of the findings found in literature. At the present site, potentially from error-prone open-bottom pipe infiltration tests, hydraulic conductivity may have been overestimated and, subsequently, infiltration rates may have been overestimated. Potential effects on the correlation may have originated from different measurement support volumes of the EMI sensor and the infiltrometer pipe. The introduction of clusters for different EC_a value ranges seems effective, to some extent, to delineate the main infiltration zone in line with the main infiltration zone from stream loss data. Further constraining field data could help to resolve these deviations. To overcome the limitations of predicting K_v from EMI-derived bulk EC_a, additional (spectral) induced polarization measurements could potentially aid to differentiate the relative contribution of electrical conductance from the pore volume pathway and from the pore surface area pathway, to EC_a.

6. References

Allred, B.J., Ehsani, M.R., Saraswat, D., 2005. The impact of temperature and shallow hydrologic conditions on the magnitude and spatial pattern consistency of electromagnetic induction measured soil electrical conductivity. Trans. Am. Soc. Agric. Eng. 48 (6), 2123–2135.

Archie, G.E., 1942. The electrical resistivity log as an aid in determining some reservoir characteristics. Trans. Am. Inst. Min. Metall. Pet. Eng. 146, 54–62.

Bear, J., Cheng, A.H.-D., 2010. Modeling Groundwater Flow and Contaminant Transport. Springer Science & Business Media.

Bernabe´ Y, Revil A (1995) Pore-scale heterogeneity, energy dissipation and the transport properties of rocks. Geophys Res Lett 22(12):1529–1532

Bertin C, Bourg ACM. 1994. Radon-222 and chloride as natural tracers of the infiltration of river water into an alluvial aquifer in which there is significant river/groundwater mixing. Environmental Science and Technology 28: 794–798.Bouwer H, Maddock T III (1997) Making sense of the interaction between groundwater and streamflow: lessons for watermasters and adjudicators. Rivers 6(1):19–31

Bichler, A., Muellegger, C., Brünjes, R., & Hofmann, T. (2016). Quantification of river water infiltration in shallow aquifers using acesulfame and anthropogenic gadolinium. Hydrological Processes, 30(11), 1742–1756

Bichler, A., Neumaier, A., & Hofmann, T. (2014). A tree-based statistical classification algorithm (CHAID)for identifying variables responsible for the occurrence of faecal indicator bacteria during waterworks operations. Journal of Hydrology, 519(Part A), 909–917

Binley, A., S. Henry-Poulter, and B. Shaw (1996), Examination of solute transport in an undisturbed oil column using electrical resistance tomography, Water Resour. Res., 32(4), 763–769.

Binley, A., S. Ullah, A. L. Heathwaite, C. Heppell, P. Byrne, K. Lansdown, M. Trimmer, and H. Zhang (2013), Revealing the spatial variability of water fluxes at the groundwater-surface water interface, Water Resour. Res., 49, 3978–3992, doi:10.1002/wrcr.20214.

Binley, A., Hubbard, S. S., Huisman, J. A., Revil, A., Robinson, D. A., Singha, K., & Slater, L. D. (2015). The emergence of hydrogeophysics for improved understanding of subsurface processes over multiple scales. Water Resources Research, 51(6), 3837– 3866.

Boucher, M., Favreau, G., Nazoumou, Y., Cappelaere, B., Massuel, S., & Legchenko, A. (2012). Constraining groundwater modeling with magnetic resonance soundings. Ground Water, 50(5), 775–784.

Bouwer, H., & Maddock, T. I. I. I. (1997). Making sense of the interactions between groundwater and streamflow: lessons for water masters and adjudicators. Rivers, 6(1), 19-31.

Bouwer, H., 2002. Artificial Recharge of Groundwater: Hydrogeology and Engineering. Hydrogeology Journal, 10(1):121-142.

Brevik, E.C., Fenton, T.E., 2002. The relative influence of soil water, clay, temperature, and carbonate minerals on soil electrical conductivity readings with an EM-38 along a Mollisol catena in central Iowa. Soil Surv. Horiz. 43, 9–13.

Brevik, E.C., Fenton, T.E., Lazari, A., 2006. Soil electrical conductivity as a function of soil water content and implications for soil mapping. Precis. Agric. 7, 393–404.

Briggs, L.J., 1899. Electrical instruments for determining the moisture, temperature, and soluble salts content of soils. USDA Div. Soils Bull. 10, U.S. Gov. Print. Office, Washington, DC.

Brice, J. C. (1964). Channel patterns and terraces of the Loup Rivers in Nebraska. Washington: U.S. Govt. Print. Off.

Brosten, T. R., F. D. Day-Lewis, G. M. Schultz, G. P. Curtis, and J. W. Lane Jr. (2011), Inversion of multi-frequency electromagnetic induction data for 3D characterization of hydraulic conductivity, J. Appl. Geophys., 73(4), 323–335.

Brunner, P., Cook, P. G., & Simmons, C. T. (2009). Hydrogeologic controls disconnection between surface water and groundwater. Water Resources Research, 45(1), 1–13.

Brünjes, R., Bichler, A., Hoehn, P., Lange, F. T., Brauch, H.-J., & Hofmann, T. (2016). Anthropogenic gadolinium as a transient tracer for investigating river bank filtration. Science of The Total Environment, 571, 1432–1440.

Camporese, M., Cassiani, G., Deiana, R., & Salandin, P. (2011). Assessment of local hydraulic properties from electrical resistivity tomography monitoring of a threedimensional synthetic tracer test experiment. Water Resources Research, 47(12), 1–15.

Cannon, M.E., McKenzie, R.C., Lachapelle, G., 1994. Soil salinity mapping with electromagnetic induction and satellite-based navigation methods. Can. J. Soil Sci. 74, 335–343.

Cardenas, M.B. and Zlotnik, V.A. (2003) Three-dimensional model of modern channel bend deposits, Water Re-sources Research, 39(6), 1141, doi:10.1029/2002WR001383.

Cardenas, M.B., Wilson, J.L. and Zlotnik, V.A. (2004) Impact of heterogeneity, bed forms, and stream curvature on subchannel hyporheic exchange, *Water Resources Research*, 40, W08307, doi:10.1029/2004WR003008.

Carter, L.M., Rhoades, J.D., Cesson, J.H., 1993. Mechanization of soil salinity assessment for mapping. Winter Meetings of the American Society of Agricultural Engineers, Paper No. 93-1557. American Society of Agricultural Engineers, St. Joseph, Michigan.

Chen, X.H., 2000. Measurement of streambed hydraulic conductivity and its anisotropy. Environmental Geology 39 (12), 1317–1324.

Chen XH. 2005. Statistical and geostatistical features of streambed hydraulic conductivities in the Platte River, Nebraska. Environmental Geology 48: 693–701.

Chen, X., Burbach, M., and Cheng, C. (2008) Electrical and hydraulic vertical variability in channel sediments and its effects on streamflow depletion due to groundwater extraction, *Journal of Hydrology*, 352, 250-266.

Cook, P. G., and S. Kilty (1992), A helicopter-borne electromagnetic survey to delineate groundwater recharge rates, Water Resour. Res., 28(11), 2953–2961, doi:10.1029/92WR01560.

Cook, P.G., Walker, G.R., 1992. Depth profiles of electrical conductivity from linear combinations of electromagnetic induction measurements. Soil Sci. Soc. Am. J. 56, 1015–1022.

Cook, P.G., Hughes, M.W.,Walker, G.R., Allison, G.B., 1989a. The calibration of frequencydomain electromagnetic induction meters and their possible use in recharge studies. J. Hydrol. 107, 51–265.

Cook, P.G., Walker, G.R., Jolly, I.D., 1989b. Spatial variability of groundwater recharge in a semiarid region. J. Hydrol. 111, 195–212.

Corwin, D.L., Rhoades, J.D., 1982. An improved technique for determining soil electrical conductivity — depth relations from above ground electromagnetic induction measurements. Soil Sci. Soc. Am. J. 46, 517–520.

Corwin, D.L., Lesch, S.M., 2003. Application of soil electrical conductivity to precision agriculture: theory,principles, and guidelines. Agron. J. 95 (3), 455–471.

Corwin, D.L., and Plant, R.E., Eds., Applications of apparent soil electrical conductivity in precision agriculture, Comput. Electron. Agric.,46, 1-10, 2005

Corwin, D.L., 2008. Past, present, and future trends in soil electrical conductivitymeasurements using geophysical methods. In: Allred, B.J., Daniels, J.J., Ehsani, M.R. (Eds.), Handbook of

Agricultural Geophysics. CRC Press, Taylor and Francis Group, Boca Raton, Florida, pp. 17–44.

Crosbie, R.S., Taylor, A.R., Davis, A.C., Lamontagne, S., Munday, T., 2014. Evaluation of infiltration from losing-disconnected rivers using a geophysical characterisation of the riverbed and a simplified infiltration model. J. Hydrol. 508, 102–113.

Daily, W., A. Ramirez, D. LaBrecque, and J. Nitao (1992), Electrical resistivity tomography of vadose water movement, Water Resour. Res., 28(5), 1429–1442.

Datry, T., Lamouroux, N., Thivin, G., Descloux, S., and Baudoin, J. M. (2015) Estimation of Sediment Hydraulic Conductivity in River Reaches and its Potential Use to Evaluate Streambed Clogging. River Res. Applic., 31: 880–891

de Jong, E., Ballantyne, A.K., Cameron, D.R., Read, D.L., 1979. Measurement of apparent electrical conductivity of soils by an electromagnetic induction probe to aid salinity surveys. Soil Sci. Soc. Am. J. 43, 810–812.

Doolittle, J., Brevik, E.C., 2014. The use of electromagnetic induction techniques in soils studies. Geoderma 223–225, 33–45.

Domenico PA, Schwartz FW (1998) Physical and chemical hydrogeology, 2nd edn. Wiley, New York

Dorn, C., N. Linde, T. Le Borgne, O. Bour, and L. Baron (2011), Single-hole GPR reflection imaging of solute transport in a granitic aquifer, Geophys. Res. Lett., 38, L08401, doi:10.1029/2011GL047152.

Dunn, B.W., Beecher, H.G., 2007. Using electro-magnetic induction technology to identify sampling sites for soil acidity assessment and to determine spatial variability of soil acidity in rice fields. Aust. J. Exp. Agric. 47, 208–214.

EEA. 2006. Corine Land Cover 2006 raster data. European Environmental Agency.

EC.2008. Groundwater Protection in Europe (The new groundwater directive – consolidating the EU regulatory framework) European Commission, Directorate-General for the Environment DOI: 10.2779/84304.

Fleckenstein, J.H., Niswonger, R.G. and Fogg, G.E. (2006) River-Aquifer Interactions, Geologic Heterogeneity, and Low-Flow Management, *Ground Water,* 44(6), 837–852.

Fox, G.A., and D.S. Durnford. 2003.Unsaturated hyporheic zone flow in stream/aquifer conjunctive systems. Advances in Water Resources 26: 989–1000.

Frei, S., Fleckenstein, J.H., Kollet, S.J. and Maxwell, R.M. (2009) Patterns and dynamics of river-aquifer exchange with variably-saturated flow using a fully-coupled model, *Journal of Hydrology,* 375, 383- 393.

Friedman, S.P. 2005. Soil properties influencing apparent electrical conductivity: A review. Computers and Electronics in Agriculture 46, no. 1–3: 45–70.

González-Pinzón, R., Ward, A. S., Hatch, C. E., Wlostowski, A. N., Singha, K., Gooseff, M. N., … Brock, J. T. (2015). A field comparison of multiple techniques to quantify groundwater–surface-water interactions. Freshwater Science, 34(1), 139–160.

Hantush, M.S. (1965) Wells near streams with semipervious beds, *Journal of Geophysical Research*, 70(12), 2829-2838.

Heigold PC, Gilkeson RH, Cartwright K, Reed PC (1979) Aquifer transmissivity from surficial electrical methods. Ground Water 17:338–345

Hiscock, K. M. (2005). Hydrogeology: Principles and practice. Malden, MA: Blackwell Pub.

Hruby, A. (2016) Viability of the Use of Electromagnetic Induction to Predict Streambed Properties. University of Nebraska - Lincoln (unpublished)

Huisman, J. A., S. S. Hubbard, J. D. Redman, and P. A. Annan (2003), Measuring soil water content with ground penetrating radar: A review, Vadose Zone J., 2(4), 476–491.

Hunt, B. (1999) Unsteady stream depletion from ground water pumping, *Ground Water*, 37(1), 98-102.

Huntley D (1986) Relations between permeability and electrical resistivity in granular aquifers. Ground Water 24:466–474

Irvine, Dylan (2010) Investigating the influence of clogging layer heterogeneity on groundwater surface water interactions for disconnected losing streams

Irvine DJ, Brunner P, Franssen HJH, Simmons CT. (2012). Heterogeneous or homogeneous? Implications of simplifying heterogeneous streambeds in models of losing streams. Journal of Hydrology 424–425: 16–23.

James, I.T.,Waine, T.W., Bradley, R.I., Taylor, J.C., Godwin, R.J., 2003. Determination of soil type boundaries using electromagnetic induction scanning techniques. Biosyst. Eng. 86 (4), 421–430.

Johnston, M.A., Savage, M.J., Moolman, J.H., du Pleiss, H.M., 1997. Evaluation of calibration methods for interpreting soil salinity from electromagnetic induction measurements. Soil Sci. Soc. Am. J. 61, 1627–1633.

Kean, W.F., Jennings Walker, M., Layson, H.R., 1987. Monitoring moisture migration in the vadose zone with resistivity. Ground Water 25, 562–571.

Kelly WE (1977) Geoelectric sounding for estimating aquifer hydraulic conductivity. Ground Water 15(6):420–425

Kemper, K.E. (2004) Groundwater–from development to management. Hydrogeology Journal 12, 3-5.

Khan, S., Rana, T., Dassanayake, D., Abbas, A., Blackwell, J., Akbar, S., Gabriel, H.F., 2009. Spatially distributed assessment of channel seepage using geophysics and artificial intelligence. Irrig. Drain. 58, 307–320.

Koestel, J., A. Kemna, M. Javaux, A. Binley, and H. Vereecken (2008), Quantitative imaging of solute transport in an unsaturated and undisturbed soil monolith with 3-D ERT and TDR, Water Resour. Res., 44, W12411, doi:10.1029/2007WR006755.

Korsaeth, A., Riley, H., Kværnø, S.H., Vestgarden, L.S., 2008. Relations between a commercial soil survey map based on apparent electrical conductivity (ECa) and measured soil properties on a moronic soil in southeast Norway. In: Allred, B.J., Daniels, J.J., Ehsani, M.R. (Eds.), Handbook of Agricultural Geophysics. CRC Press, Taylor and Francis Group, Boca Raton, Florida, pp. 225– 231.

Kurtz, W., Hendricks Franssen, H.-J., Brunner, P., & Vereecken, H. (2013). Is high-resolution inverse characterization of heterogeneous river bed hydraulic conductivities needed and possible? Hydrology and Earth System Sciences, 17(10), 3795–3813.

Lambot, S., L. Weihermuller, J. A. Huisman, H. Vereecken, M. Vanclooster, and E. C. Slob (2006), Analysis of air-launched ground-penetrating radar techniques to measure the soil surface water content, Water Resour. Res., 42, W11403, doi:10.1029/2006WR005097.

Leibundgut, C., Maloszewski, P., & Külls, C. (2009). Environmental tracers. Tracers in Hydrology. Chichester: John Wiley & Sons.

Lück, E., Gebbers, R., Ruehlmann, J., Sprangenberg, U., 2009. Electrical conductivity mapping for precision farming. Near Surf. Geophys. 7 (1), 15–25.

Mankin, K.R., Karthikeyan, R., 2002. Field assessment of saline seep remediation using electromagnetic induction.Trans. ASAE 45 (1), 99–107.

McNeill, J.D., 1980. Electrical conductivity of soils and rock. Technical Note TN-5. Geonics Limited, Mississauga, Ontario, Canada.

Niwas, S., Tezkan, B., & Israil, M. (2011). Aquifer hydraulic conductivity estimation from surface geoelectrical measurements for Krauthausen test site, Germany. Hydrogeology Journal, 19(2), 307–315.

Ponzini G, Ostroman A, Molinari M (1983) Empirical relation between electrical transverse resistance and hydraulic transmissivity. Geoexploration 22:1–15

Purvance DT, Andricevic R (2000) Geoelectric characterization of the hydraulic conductivity field and its spatial structure at variable scales. Water Resour Res 36(10):2915–2924

Regli C, Rauber M, Huggenberger P. 2003. Analysis of aquifer heterogeneity within a well capture zone, comparison of model data with field experiments: a case study from the river Wiese, Switzerland. Aquatic Sciences 65: 111–128.Schaelchli, U. (1993). Berechnungsgrundlagen der inneren Kolmation von Fliessgewaessersohlen. Wasser, Energie, Luft, 85, 321-331.

Rhoades, J.D., Corwin, D.L., Lesch, S.M., 1999a. Geospatial measurements of soil electrical conductivity to assess soil salinity and diffuse salt loading from irrigation. In: Corwin, D.L., Loague, K., Ellsworth, T.R. (Eds.), Assessment of Non-point Source Pollution in theVadose Zone. Geophysical Monograph 108. American Geophysical Union, Washington, DC, USA, pp. 197–215

Rhoades, J.D., Corwin, D.L., 1981. Determining soil electrical conductivity-depth relations using an inductive electromagnetic soil conductivity meter. Soil Sci. Soc. Am. J. 45, 255–260.

Richardson, D.P., Williams, B.G., 1994. Assessing discharge characteristics of upland landscapes using electromagnetic induction techniques. Technical Memorandum 94/3. CSIRO Institute of Natural Resources and Environment, Division of Water Resources, Canberra, Australia.

Saey, T., De Smedt, P., De Clercq, W., Meerschman, E., Islam, M.M., Van Meirvenne, M., 2012a. Identifying soil patterns at different spatial scales with a multi-receiver EMI sensor. Soil Sci. Soc. Am. J. 77, 382–390.

Scanlon, B.R., Paine, J.G., Goldsmith, R.S., 1999. Evaluation of electromagnetic induction as a econnaissance technique to characterize unsaturated flow in an arid setting. Ground Water 37 (2), 296–304.

Schneider, S., Mallants, D., & Jacques, D. (2012). Determining hydraulic properties of concrete and mortar by inverse modelling. MRS Proceedings, 1475. doi:10.1557/opl.2012.601Sen PN, Scala C, Cohen MH (1981) A self-similar model for sedimentary rocks with application to the dielectric constant of fused glass beads. Geophysics 46:781–795

Şen, Z. (2015). Practical and applied hydrogeology. Elsevier.

Sheets, K.R., Hendrickx, J.M.H., 1995. Noninvasive soil water content measurements using electromagnetic induction. Water Resour. Res. 31, 2401–2409.

Singha, K., and S. M. Gorelick (2005), Saline tracer visualized with three-dimensional electrical resistivity tomography: Field-scale spatial moment analysis, Water Resour. Res., 41, W05023, doi:10.1029/2004WR003460.

Slater, L. D., D. Ntarlagiannis, F. D. Day-Lewis, K. Mwakanyamale, R. J. Versteeg, A. Ward, C. Strickland, C. D. Johnson, and J. W. Lane Jr. (2010), Use of electrical imaging and distributed temperature sensing methods to characterize surface water-groundwater exchange regulating uranium transport at the Hanford 300 Area, Washington, Water Resour. Res., 46, W10533, doi:10.1029/2010WR009110.

Sophocleous, M. 2002. Interactions between groundwater and surface water: The state of the science. Hydrogeology Journal 10: 52–67.

Spies, B.R., 1989. Effective depth of exploration in electromagnetic sounding methods. Geophysics 54, 872–888.

Springer, A. E., Petroutson, W. D., & Semmens, B. A. (1999). Spatial and temporal variability of hydraulic conductivity in active reattachment bars of the Colorado River, Grand Canyon. Ground Water, 37(3), 338–344.

Theis, C.V. (1941) The effect of a well on the flow of a nearby stream, *American Geophysical Union Transactions,* 22(3), 734-738.

Topp, G. C., J. L. Davis, and A. P. Annan, 1980. Electromagnetic determination of soil water content: Measurements in coaxial transmission lines, Water Resour. Res., 16(3), 574–582.

Treese, S., Meixner, T. and Hogan, J. F. (2009), Clogging of an Effluent Dominated Semiarid River: A Conceptual Model of Stream-Aquifer Interactions1. JAWRA Journal of the American Water Resources Association, 45: 1047–1062. doi:10.1111/j.1752-1688.2009.00346.x

Triantafilis, J., Lesch, S.M., La Lau, K., Buchanan, S.M., 2009. Field level digital mapping of cation exchange capacity using electromagnetic induction and a hierarchical spatial regression model. Aust. J. Soil Res. 47, 651–663.

Turnadge, C., & Smerdon, B. D. (2014). A review of methods for modelling environmental tracers in groundwater: advantages of tracer concentration simulation. Journal of Hydrology, 519(Part D), 3674–3689

Veličković, B. (2005). Colmation as one of the processes in interaction between the groundwater and surface water. Factas Universitatis. Architecture and Civil Engineering Vol. 3, No 2, 2005, pp. 165 – 172.

Vitharana, U.W.A., Saey, T., Cockx, L., Simpson, D., Vermeersch, H., Van Meirvenne, M., 2008. Upgrading a 1/20,000 soil map with an apparent electrical conductivity survey. Geoderma 148, 107–112.

Wenner, F., 1915. A method of measuring Earth resistivity. U.S. Dept. Com. Bureau of Standards Sci. Paper No. 258. NIST, Gaithersburg, MD.

White, M.L., Shaw, J.N., Raper, R.L., Rodekohr, D., Wood, C.W., 2012. A multivariate approach for high-resolution soil survey development. Soil Sci. 177 (5), 345–354.

Wienhold, B.J., Doran, J.W., 2008. Apparent electrical conductivity for delineating spatial variability in soil properties. In: Allred, B.J., Daniels, J.J., Ehsani, M.R. (Eds.), Handbook of Agricultural Geophysics. CRC Press, Taylor and Francis Group, Boca Raton, Florida, pp. 211–215.

Williams, B.G., Baker, G.C., 1982. An electromagnetic induction technique for reconnaissance surveys of soil salinity hazards. Aust. J. Soil Res. 20, 107–118.

Williams, B., Walker, J., Anderson, J., 2006. Spatial variability of regolith leaching and salinity in relation to whole farm planning. Aust. J. Exp. Agric. 46, 1271–1277.

Winter, T.C., J.W. Harvey, O.L. Franke, and W.M. Alley. 1998. Ground Water and Surface Water A Single Resource, Circular 1139. Denver: Colorado: USGS.

List of Tables

List of Figures